Influence of NO_x, SO_2 and benzene on the formation of secondary organic aerosol from naphthalene - Supplementary Information

Merve Polat[1,2,*], Amir Ben Brik[3,*], Niall O'Sullivan[3], Mixtli Campos-Pineda[5], Albert A. Ruth[5], John Wenger[3], Jakob K. Nøjgaard[1,2,6], and Matthew S. Johnson[1,4]

[1]National Research Centre for the Working Environment, DK-2100 Copenhagen, Denmark
[2]Department of Chemistry, University of Copenhagen, DK-2100 Copenhagen, Denmark
[3]School of Chemistry and Sustainability Institute, University College Cork, T12 YN60 Cork, Ireland
[4]Luper Technologies, NL-5656 AE Eindhoven, Netherlands
[5]School of Physics and Sustainability Institute, University College Cork, T12 YN60 Cork, Ireland
[6]Department of Environmental Science, Aarhus University, DK-4000 Roskilde, Denmark
[*]*These authors contributed equally*

Contents

S1 Irish Atmospheric Simulation Chamber (IASC) S2

S1.1 Chamber Wall loss and UVAB lamps S2

S2 Particle coagulation rates, particle bin growth rates and particle modes S4

S2.1 Coagulation rates, r_{coag} S5

S2.2 Growth rates, r_{growth} S7

S2.3 Particle size distribution modes S8

S3 Initial experimental conditions, and the estimation of the OH concentration and production rate S10

S3.1 Multi-linear regression model based on the stable pre-UV signal S12

S3.2 Naphthalene-decay derived OH concentration S17

S3.3 Estimation of atmospheric aging from predicted OH S18

S3.4 Empirical OH estimation, and the calculation of the OH production rate S19

S3.5 Production rate of OH, r_{OH} S20

S4 Time-series for each experiment and overview tables S21

S4.1 Experiment time-series S22

S5 Comparison with the literature S38

S1 Irish Atmospheric Simulation Chamber (IASC)

S1.1 Chamber Wall loss and UVAB lamps

Two important factors affecting the experiments are wall diffusion and the UV lamps (Figure S4). The walls of the Teflon-foil chamber act as a sink for particles; it is therefore important to quantify particle uptake by the walls. This was investigated in a dedicated wall-loss experiment, where ammonium sulfate aerosol was generated by atomising a 0.015 M solution using a TSI 3076 atomiser. The generated particles were dried and neutralised before entering the chamber. The experiment was conducted by injecting particles into the chamber and then switching to "Experiment mode" with the fans on to observe how the plume evolves under mixing. Figure S1 shows the time series. The plume maximum at 12:11-12:12 was used as the initial condition, and the subsequent evolution and particle loss are shown in Figures S2 and S3, respectively.

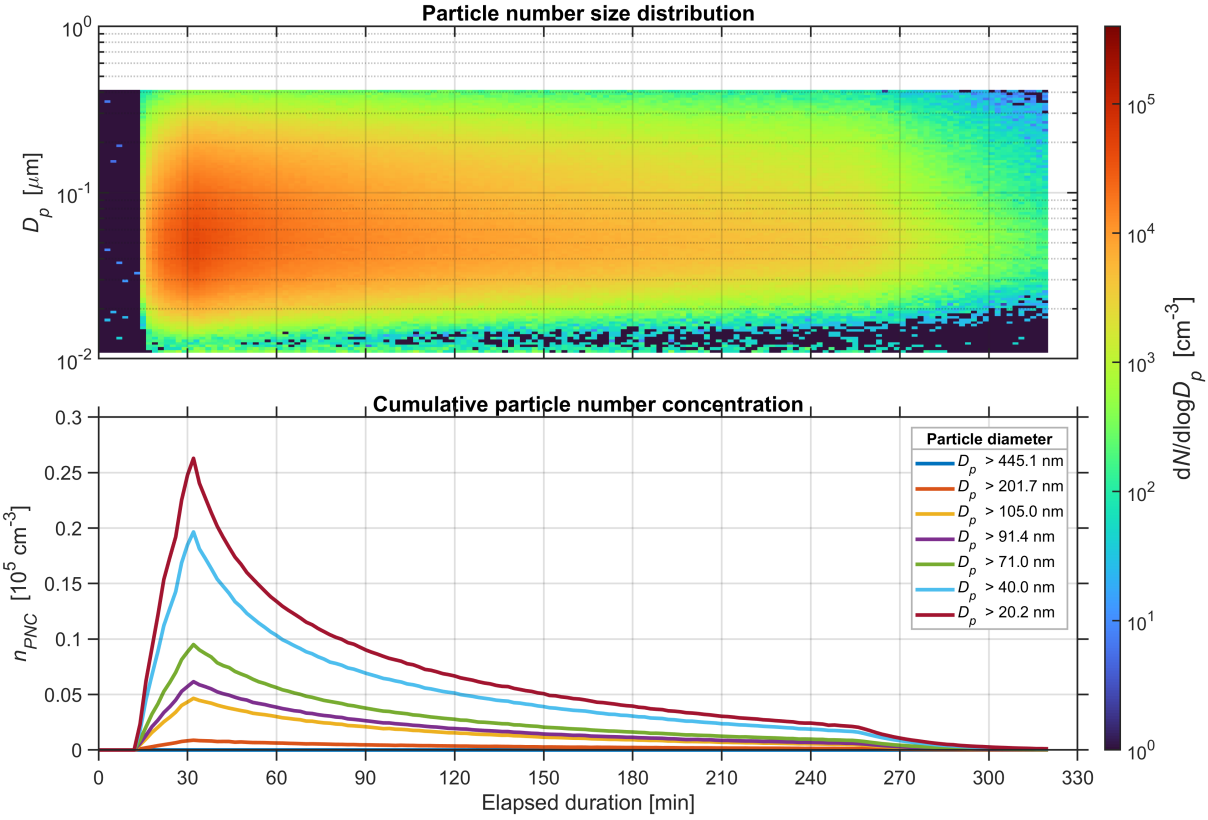


Figure S1. Wall-loss experiment with seed particles added into the chamber. The figure shows the particle number size distribution (PNSD) and the particle number concentration (PNC) as a function of time.

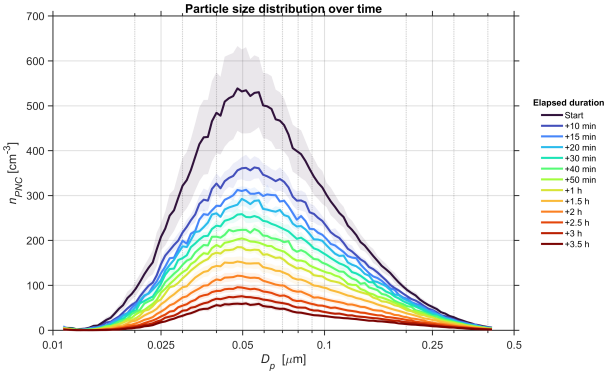


Figure S2. Particle number concentration as a function of particle diameter. The different lines show how dN evolves with time in the chamber.

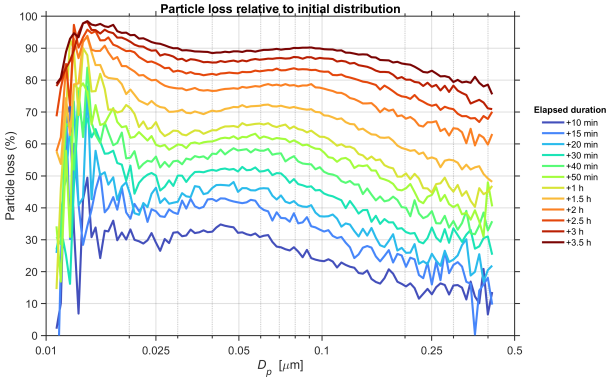


Figure S3. Particle loss between 10 min and 3.5 h shown as a function of particle diameter. After 10 min, approximately 70-80% of particles remain, while after 1 h the particle number concentration is approximately halved.

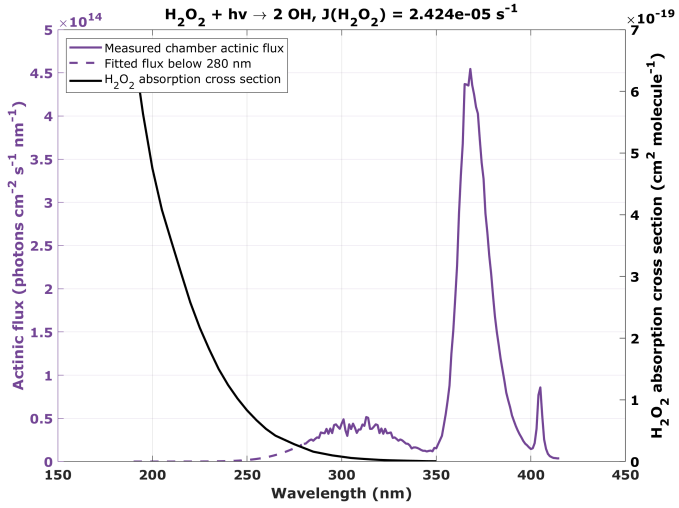


Figure S4. Absorption cross section for H_2O_2 from Burkholder et al. (2015). The quantum yield used to calculate the photolysis rate was set to 1.1 following Goldstein et al. (2007).

S2 Particle coagulation rates, particle bin growth rates and particle modes

From the SMPS measurements, in addition to particle mass and number concentrations, three particle-dynamics parameters were calculated: the total **coagulation rate**, the **growth rate**, and the evolution of **particle number distribution modes**.

Particle number concentration (n_{PNC}) and particle mass concentration (attributed to secondary organic aerosol, m_{SOA}) are presented for Experiments 1-26 in Figures S5 and S6.

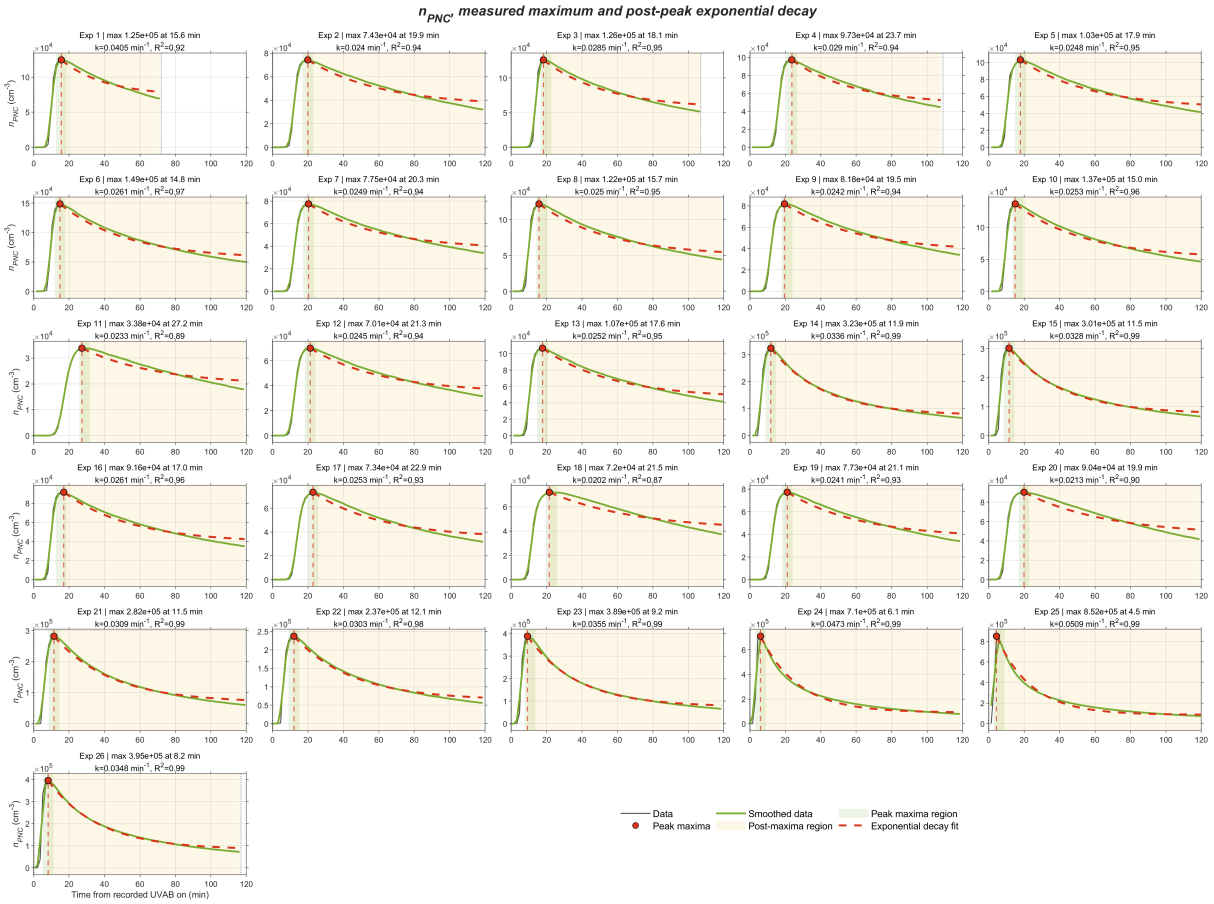


Figure S5. Particle number concentration, n_{PNC}, as a function of time after UVAB was switched on for Experiments 1-26. For each experiment, the maximum and its occurrence time are marked, and the exponential decay from the maximum is shown as well.

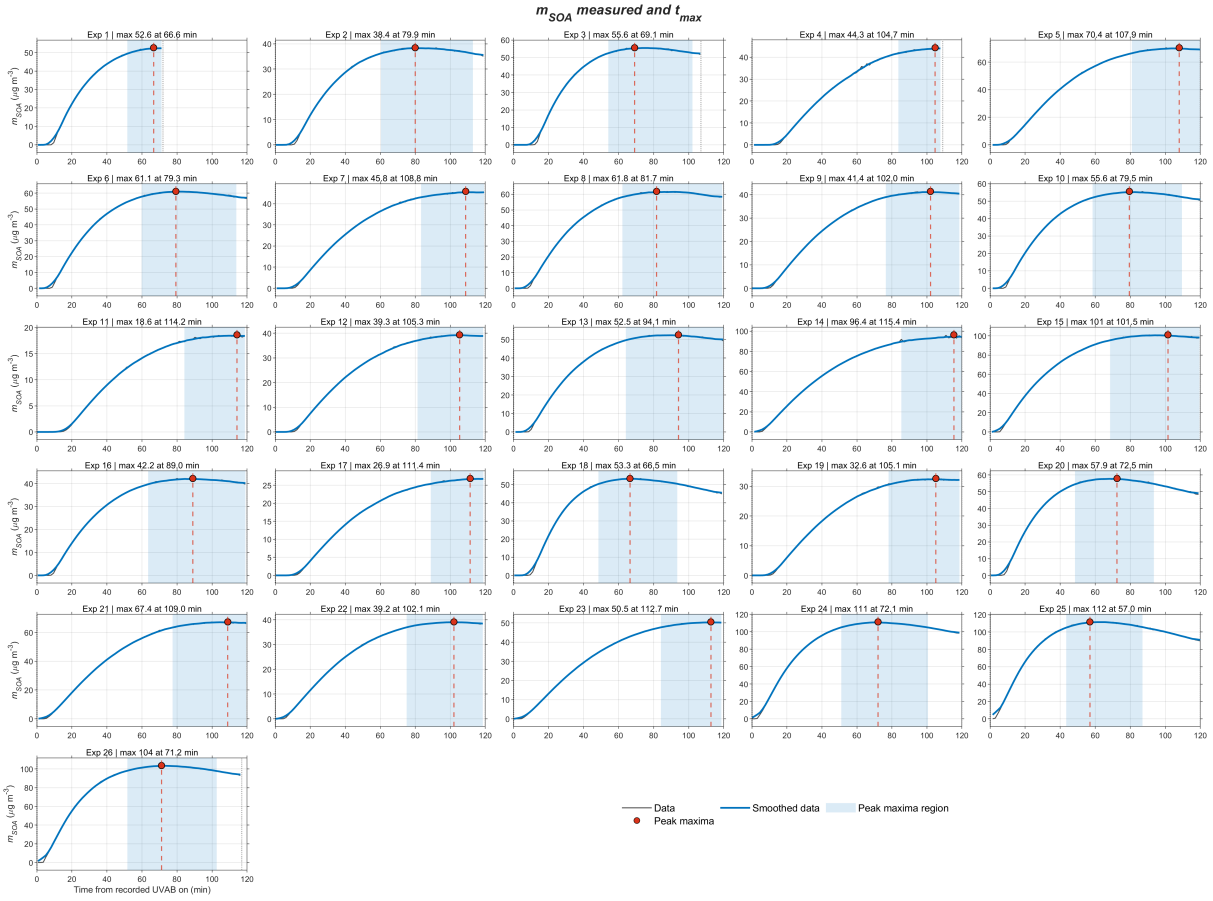


Figure S6. Particle mass concentration, m_{SOA}, as a function of time after UVAB was switched on for Experiments 1-26. For each experiment, the maximum and its occurrence time are marked (t_{max}).

S2.1 Coagulation rates, r_{coag}

The coagulation rate is calculated using Eqs. 13.45, 13.47, and 13.50 from Seinfeld and Pandis 2016. The coagulation rate affecting particles in each size class is computed as shown in Eq. 1. For each time step, the coagulation rate is calculated for each size bin interacting with every other size bin, yielding a grid similar to the number distribution. The coagulation sink for each size bin is then obtained by summing across interaction partners.

$$J_{12}(t)\,[\mathrm{cm}^{-3}\,\mathrm{s}^{-1}] = K_{12}(t)\,N_1(t)\,N_2(t) \tag{1}$$

Here N_x $(x = 1, 2)$ is the particle number concentration in size bin x, and K_{12} is the coagulation kernel, calculated from particle diffusion (D_x, Eq. 3), particle diameter (D_{px}), and the Fuchs correction factor (F_{12}), as shown in Eq. 2.

$$K_{12} = 2\pi(D_1 + D_2)(D_{p1} + D_{p2})\,F_{12} \tag{2}$$

$$D_1 = \frac{k_B\, C_c(D_{p1})}{3\pi\,\mu\, D_{p1}} \tag{3}$$

$$C_c(D_{p1}) = 1 + \frac{2\lambda}{D_{p1}}\left(1.257 + 0.4\cdot\exp\left(-\frac{1.1\cdot D_{p1}}{2\lambda}\right)\right) \tag{4}$$

The coagulation sink for particles of varying sizes is defined in Eq. 1. Here we report the summarized coagulation rate for particles a and b at each time step t as r_{coag}. The total r_{coag} is presented in Figure S7.

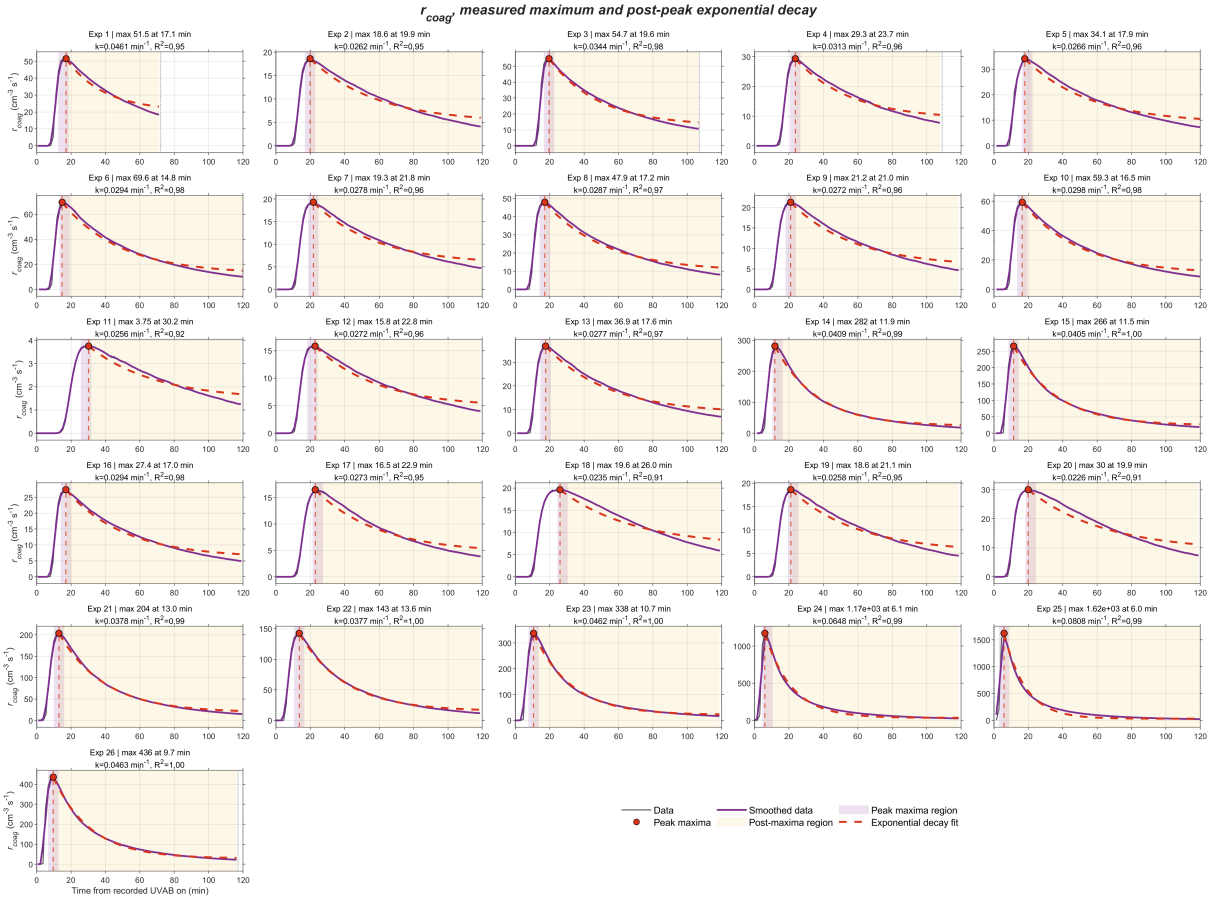


Figure S7. r_{coag} as a function of time after UVAB was switched on for Experiments 1-26. For each experiment, the maximum and its occurrence time are marked, and the exponential decay from the maximum is indicated.

S2.2 Growth rates, r_{growth}

The original SMPS size distribution consists of 102 mobility-diameter channels. Using the lower edge of the smallest bin (11.5 nm) and the upper edge of the largest bin (453.2 nm), the lower and upper bin edges were reconstructed assuming log-equidistant spacing.

To improve the signal-to-noise ratio for the nucleation mode, the 102 size channels were aggregated into seven broader size bins by summing the number size distribution over predefined index ranges (contiguous SMPS-channel clusters). For each aggregated bin, an effective midpoint diameter was defined as the geometric mean of the lower edge of the first SMPS bin in the cluster and the upper edge of the last SMPS bin in the cluster. The resulting seven time series of particle number concentration were then used for growth-rate analysis.

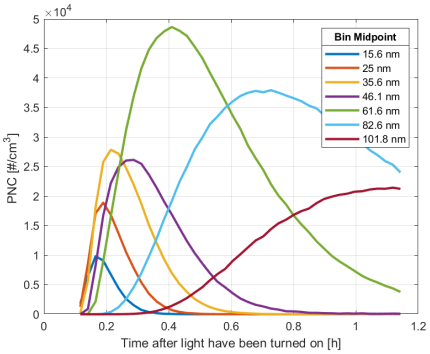


Figure S8. Particle number concentration for the seven reconstructed bins, illustrating particle evolution as a function of time after UVAB was switched on. For example, the 15.6 nm bin peaks 12 min after lights-on, while the 61.6 nm bin peaks after 25 min.

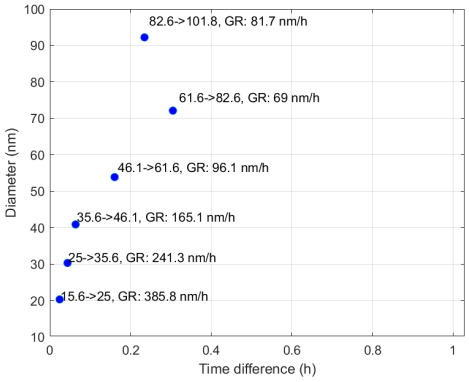


Figure S9. Growth rates between consecutive bins (e.g., 15.6 nm to 25 nm) calculated as a function of the time difference between bin-peak times.

For each of these seven aggregated bins, the temporal evolution of particle number concentration was fitted with a one-dimensional Gaussian function, as presented in Figure S8. The Gaussian center time was taken as the time of maximum occurrence for that size bin (i.e., the mean of the fitted Gaussian). Particle growth rates were then calculated between pairs of consecutive size bins. For each pair, the growth rate, r_{growth}, was defined as

$$r_{growth} = \frac{D_{p2} - D_{p1}}{t_{p2} - t_{p1}} \tag{5}$$

where D_{p2} and D_{p1} are the effective midpoint diameters of the two bins, and the corresponding center times are t_{p2} and t_{p1}. This results in the r_{growth} evolution presented in Figure S9.

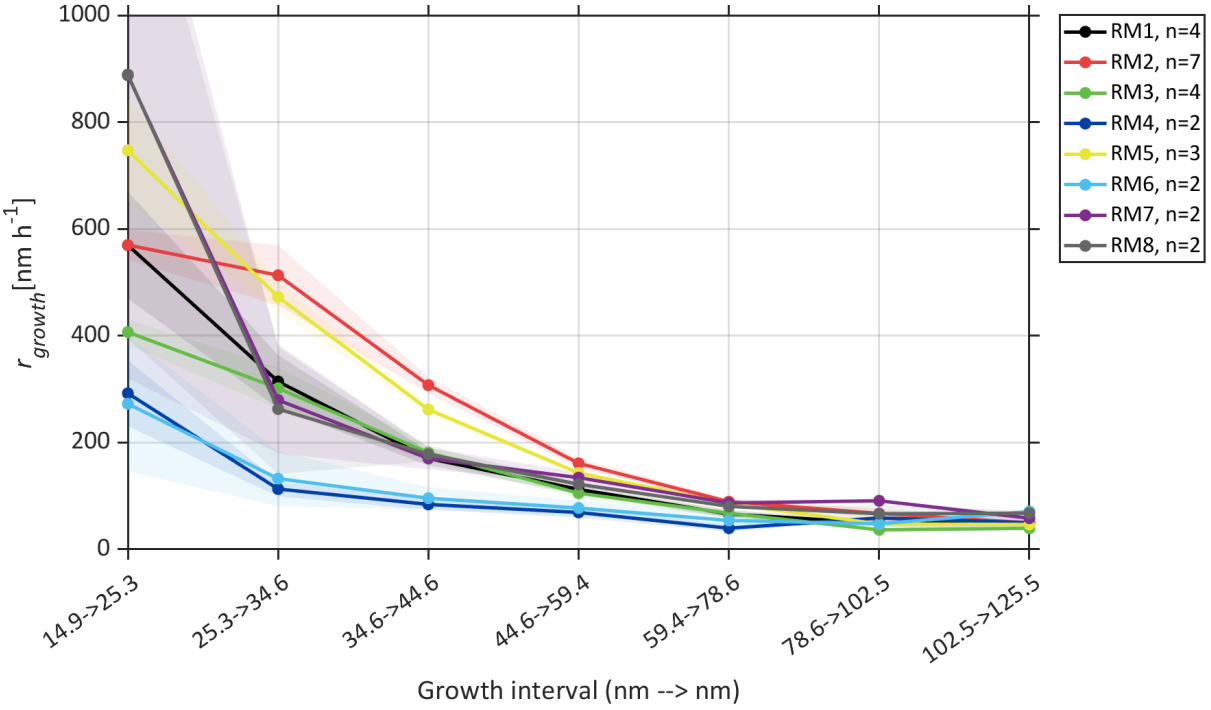


Figure S10. Growth rates calculated across the size bins indicated by the growth interval. The number of experimental replicates for each reaction mixture is shown in the legend as "$n =$".

S2.3 Particle size distribution modes

As new particles are formed from the precursor gases, the modes evolve differently in time. This can be seen in Figure S11 for the base case (RM1). Here we observe a small mode at 10-15 min post-UV that continuously grows until approximately 1 h. The mode diameter in the particle number distribution subsequently decreases, whereas for the particle mass distribution this decrease occurs later (after ~2 h). Figure S12 presents how the other reaction mixtures (RMx, $x = 2$-8) differ relative to RM1 in terms of mode diameter and mode height.

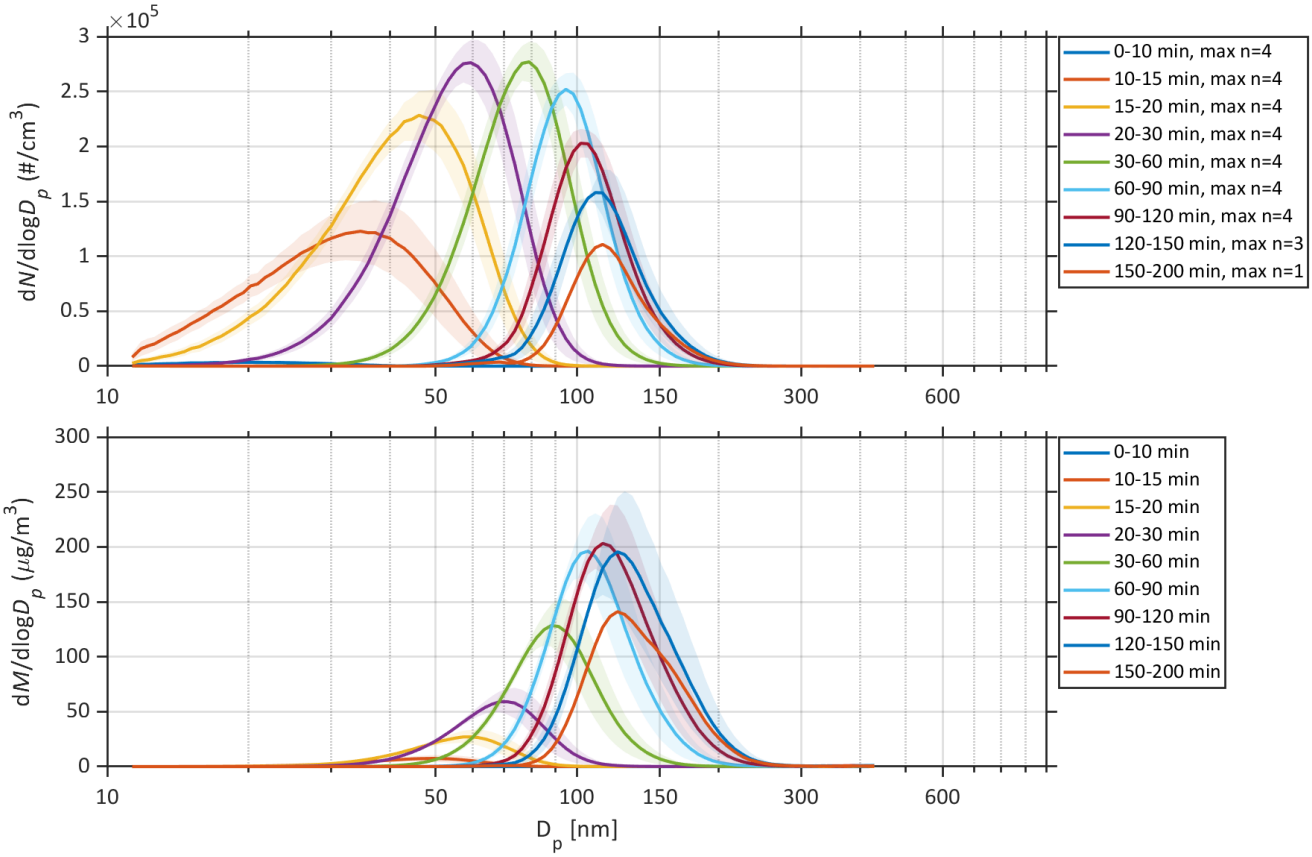


Figure S11. Post-UV time evolution of the $dN/d\log D_p$ mode for RM1 (upper panel) and the $dM/d\log D_p$ mode for RM1 (lower panel).

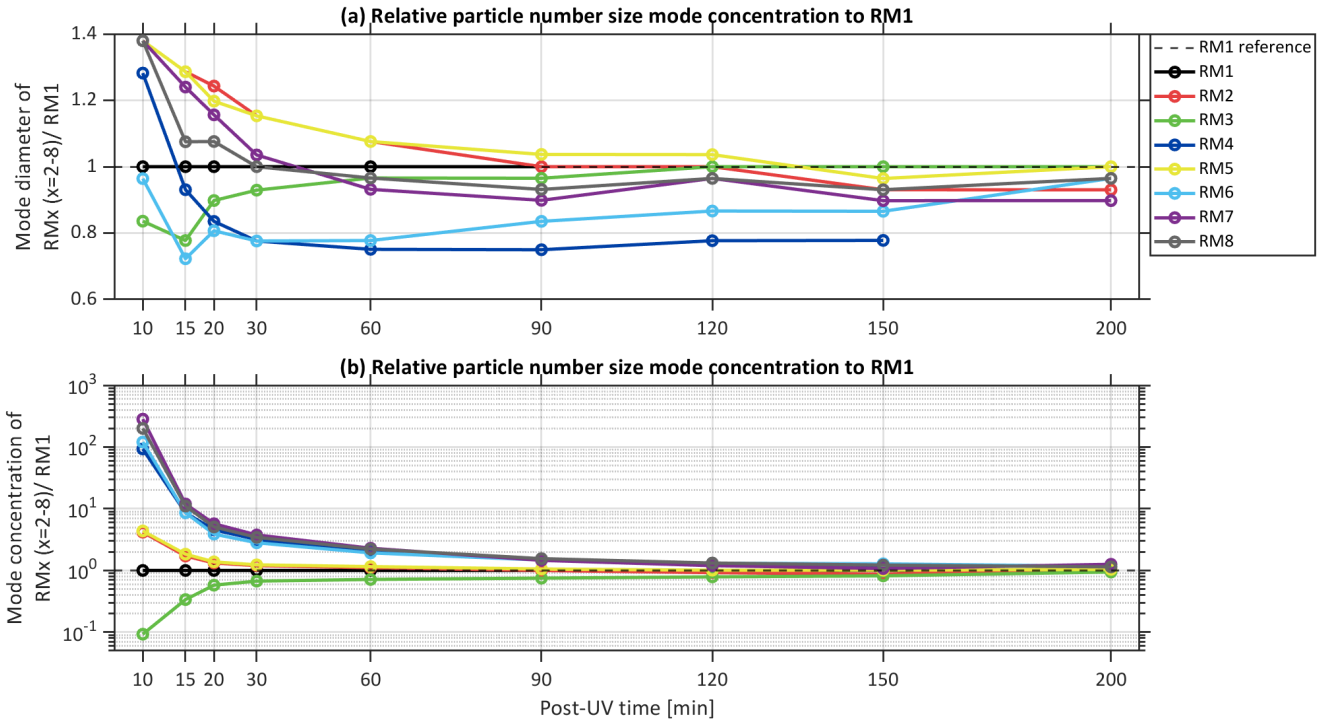


Figure S12. Evolution of the $dN/d\log D_p$ mode after UVAB was switched on. The upper panel shows the mode diameter relative to the base case (RM1) as a function of time. The lower panel shows the corresponding mode height, also relative to the base case.

S3 Initial experimental conditions, and the estimation of the OH concentration and production rate

We alternated between two ToF-CIMS ionisation modes to detect compounds that were not observable in a single mode. As a consequence, the SOA precursor naphthalene could only be measured in positive mode and was not detected in negative mode. Ten experiments were performed in positive mode (eight including naphthalene), allowing the naphthalene signal and its decay to be quantified.

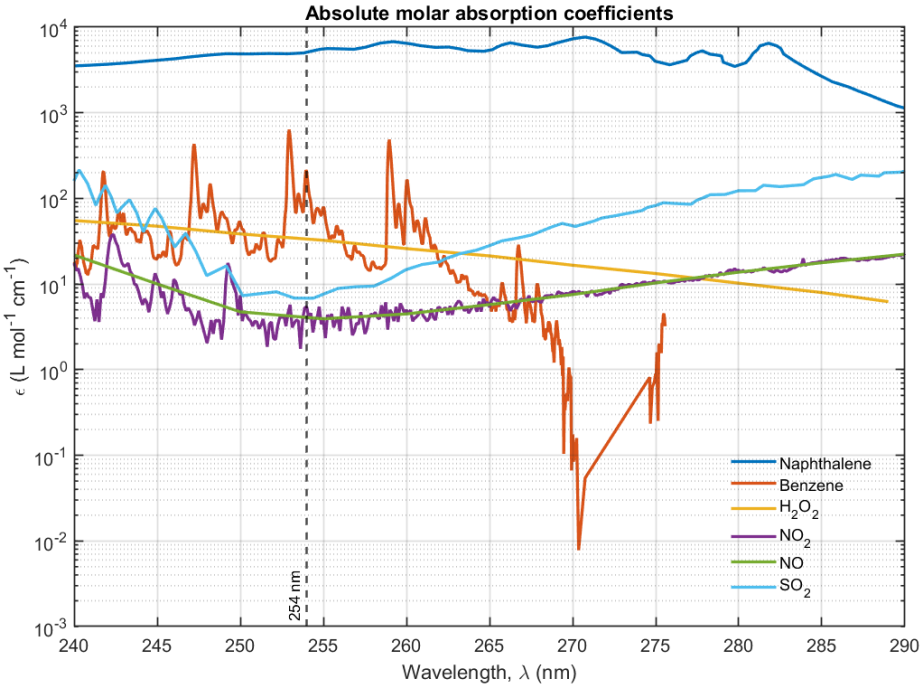


Figure S13. Absorption coefficients (from Keller-Rudek et al. (2013)) of species relevant for this study.

The Teledyne API model T400 uses a vapour mercury lamp designed so that most of the emitted radiation is centred near 254 nm. As shown in Figure S13, naphthalene, benzene, and H_2O_2 absorb strongly at this wavelength. During the pre-UV period (after gases had been introduced but before the UV lamps were switched on), an increase in the ozone signal was observed even though no ozone formation was expected in the chamber. We therefore treated the pre-light ozone signal as an interference/bias signal and constructed a multi-linear regression model based on naphthalene, benzene, H_2O_2, and relative humidity. Experiments in which these parameters were varied were used to constrain the model. The inverse form of the model was then applied to estimate the initial naphthalene and benzene concentrations for experiments in which these compounds were not measured directly (see **Multi-linear regression model based on the stable pre-UV signal**).

For one-third of the experiments run in positive mode, the observed naphthalene decay after UVAB lights-on (Figure S19) was used to derive the OH concentration (see **Naphthalene-decay derived OH concentration**). For approximately two-thirds of the experiments, however, naphthalene could not be measured directly, despite careful preparation of the injected amounts. Benzene was not measured directly in either mode.

For the experiments performed in positive mode, OH concentrations obtained from the measured naphthalene decay (Experiments 1-3, 6, and 10 also contained NO) were used as training data for an empirical prediction model. The predictors were naphthalene, benzene, H_2O_2, relative humidity, and pre-light NO. This model was subsequently used to estimate OH

concentrations for the remaining experiments (see **Empirical OH estimation, and the calculation of the OH production rate**).

S3.1 Multi-linear regression model based on the stable pre-UV signal

Pre-light ozone readings were treated as an interference/bias signal and modelled as a linear function of relevant pre-light conditions (5-30 min before lights-on). Since no lights are turned on and no ozone is injected, we interpret the ozone UV-channel readings as cross sensitivities.

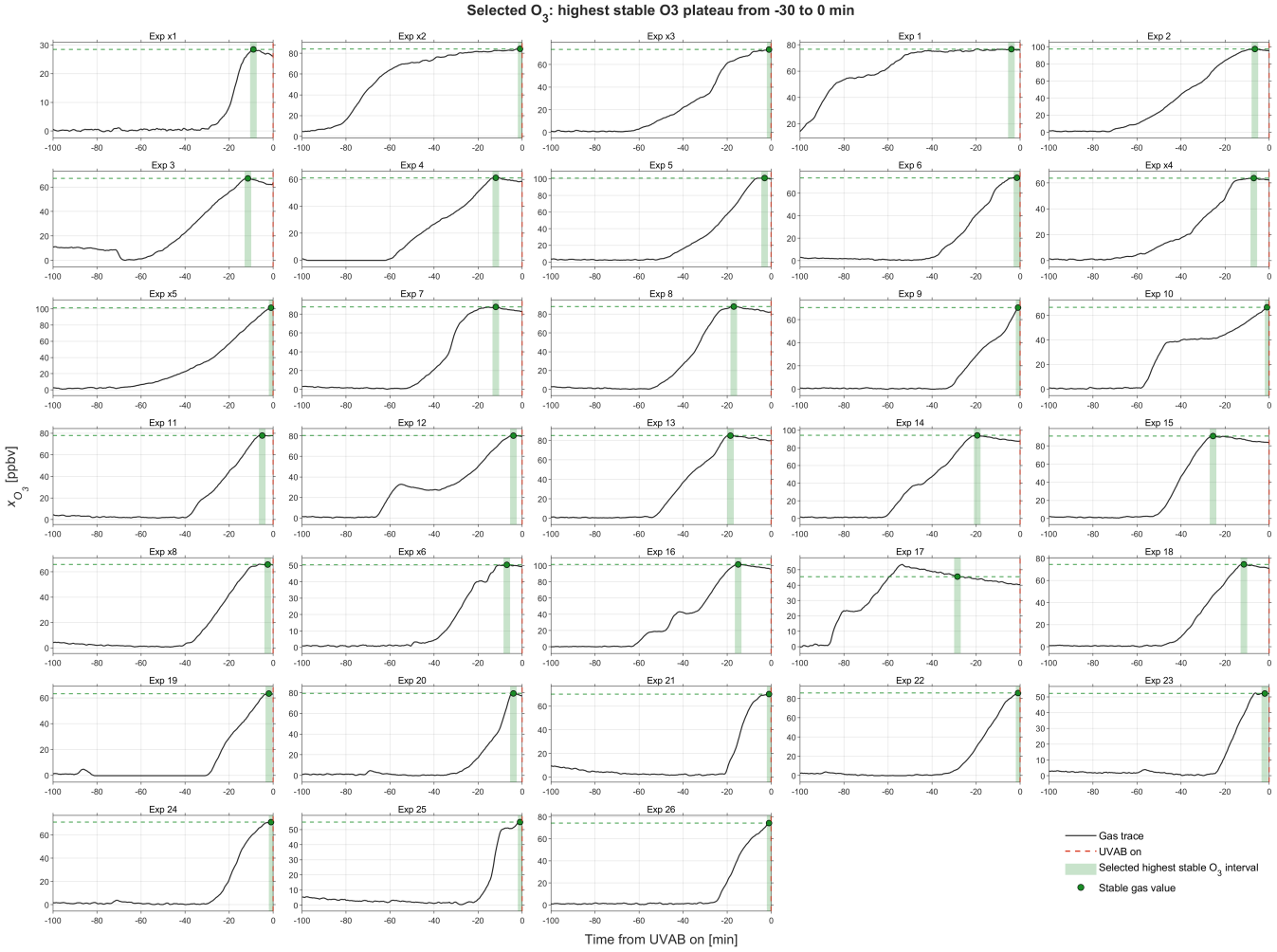


Figure S14. Stable O_3 signal pre-UV for Experiments 1-26 and additional experiments x1-x7.

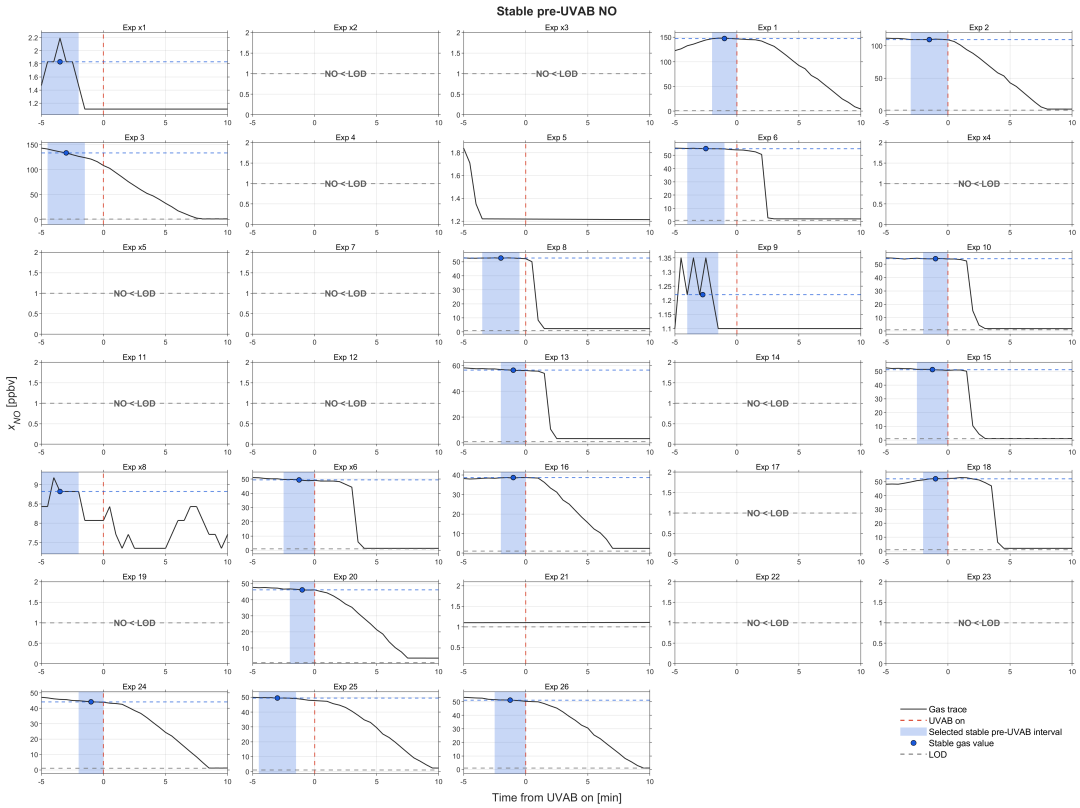


Figure S15. Stable NO signal pre-UV for all experiments.

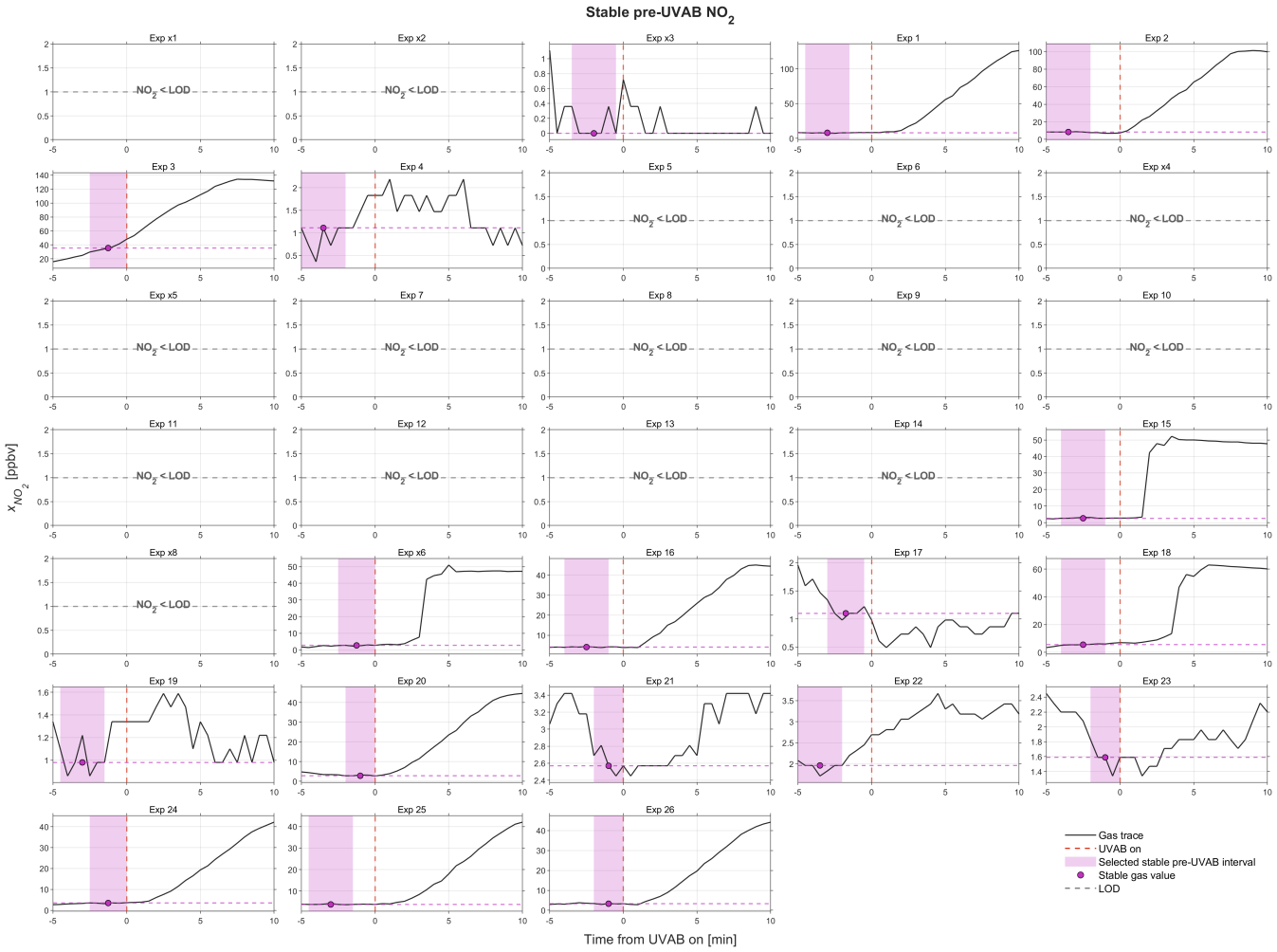


Figure S16. Stable NO_2 signal pre-UV for all experiments.

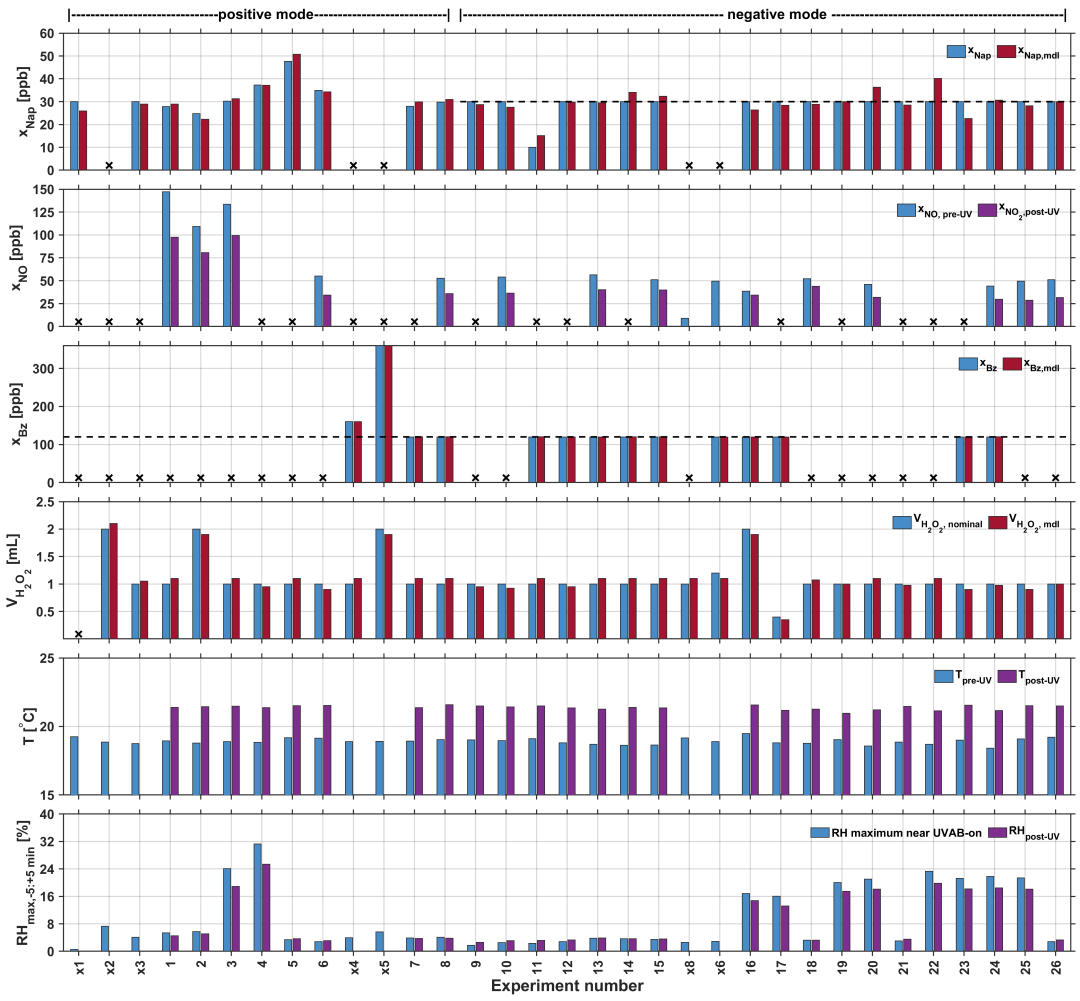


Figure S17. Summary of pre-UV conditions used as predictors in the ozone-bias model.

Using experiments with complete predictor data, an ordinary least squares model was fit, as shown in Eq. 6. H_2O_2 was included as an injected-volume proxy. Naphthalene and benzene mixing ratios (ppbv) were estimated from the injected mass (and, for naphthalene, from the positive mode when available). Relative humidity was calculated from pre-light instrument readings.

$$O_3\,\text{bias} = a_0 + a_1 \cdot x_{nap} + a_2 \cdot x_{bz} + a_3 \cdot V_{H_2O_2} + a_4 \cdot RH \tag{6}$$

where a_0 = 5.9, a_1 = 0.96 per 1 ppbv naphthalene, a_2 = 0.07 per 1 ppbv benzene, a_3 = 39.0 per 1 mL of H_2O_2, and a_4 = -0.8 per 1% RH (relative to 3.9% RH).

Figure S18 compares the estimated ozone pre-light bias and the observed O_3 signal. The model has an R^2 of 0.8, indicating that it captures a substantial fraction of the variability in the pre-UV ozone signal.

For experiments where the ToF-CIMS was operated in negative mode, no direct indication of the naphthalene amount was available. To estimate naphthalene and benzene concentrations, the fitted model was rearranged to isolate their respective regression terms from the ozone signal.

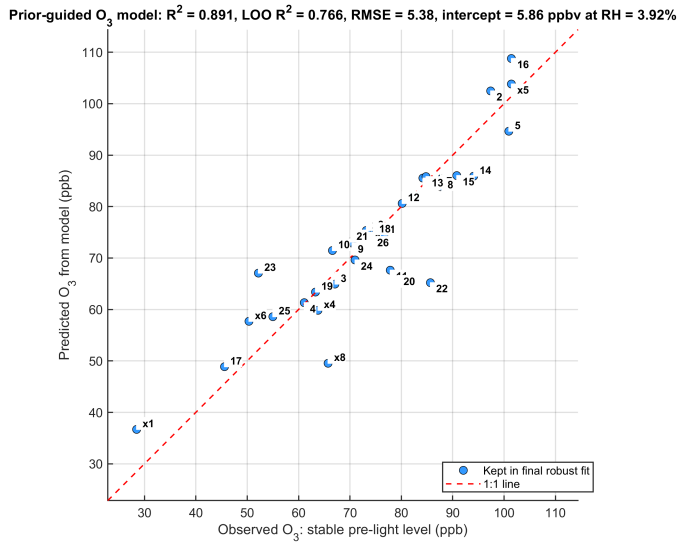


Figure S18. Comparison of model-estimated O_3 with the observed O_3 signal. The relationship is approximately linear, with a weighted R^2 of 0.7.

Figure S17 summarises the pre-UV naphthalene, benzene, and NO_2 mixing ratios. Modelled concentrations for benzene and naphthalene are reported as $x_{Nap,mdl}$ and $x_{Bz,mdl}$, respectively. The corresponding NO_2, T, and RH values at 5-30 min after lights-on are reported with subscript "hv".

S3.2 Naphthalene-decay derived OH concentration

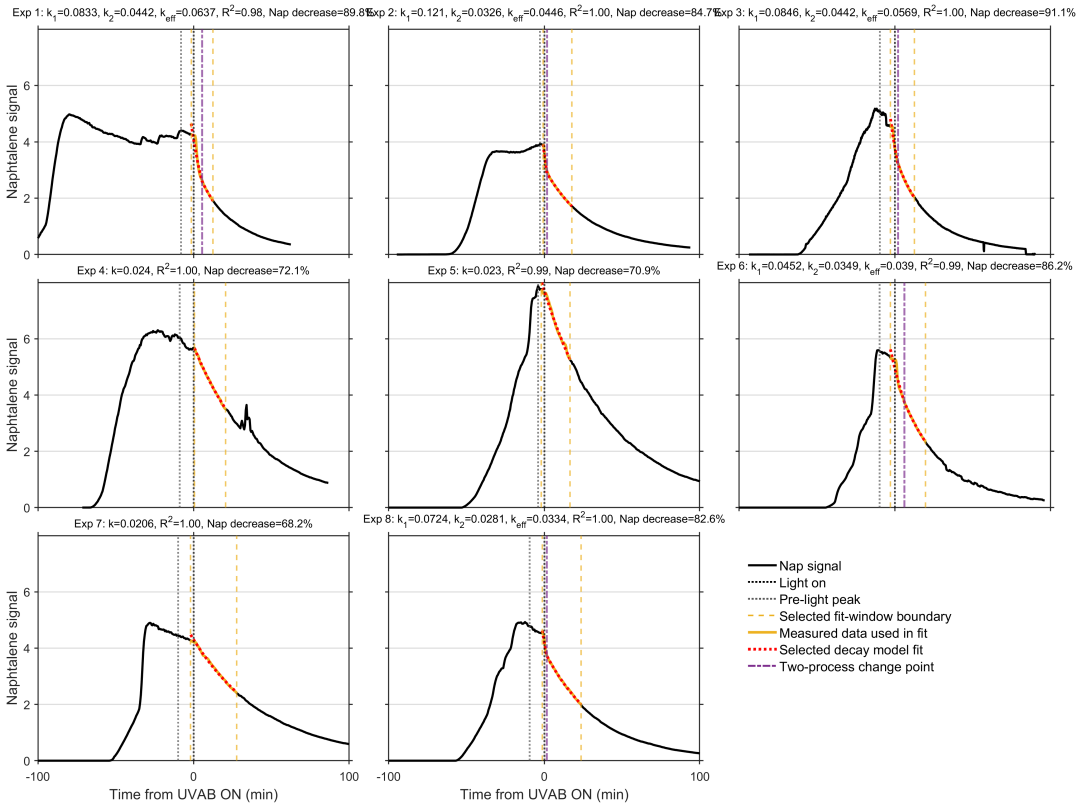


Figure S19. Naphthalene time series from ToF-CIMS and the estimated OH rate coefficient for eight experiments. Some experiments show two decay stages; in these cases an effective decay rate (k_{eff}) was calculated by integrating OH exposure across both stages and dividing by the total fitted duration.

For experiments where it was possible to measure naphthalene in the positive mode, OH concentrations were estimated from the post-light decay of the naphthalene signal assuming pseudo-first-order loss (Eqs. 7-8). The decay fit was performed only for $t > 0$ and only when more than four data points were available (Figure S19). A linear regression was applied to $\ln(\mathrm{signal})$ versus time (minutes), yielding k_{obs}. The steady-state OH concentration was calculated from Eq. 9. Because benzene also reacts with OH, Eq. 10 was used for experiments in which benzene was included.

$$\frac{d[\mathrm{Naphthalene}]}{dt} = -k_{\mathrm{obs}}\,[\mathrm{Naphthalene}] \tag{7}$$

$$\ln([\mathrm{Naphthalene}]) = \ln([\mathrm{Naphthalene}]_0) - k_{\mathrm{obs}}\,t \tag{8}$$

$$[\mathrm{OH}] = \frac{k_{\mathrm{obs}}}{k_{\mathrm{Nap+OH}}(T)} \tag{9}$$

where $k_{\mathrm{Nap+OH}}$ is 1.05×10^{-12} [cm^3 molecule^{-1} s^{-1}] $\exp\left(\frac{7.50\,(\pm 2.03\,\mathrm{kJ\ mol^{-1}})}{RT}\right)$ from Atkinson 1986.

$$[\mathrm{OH}]_{\mathrm{mix}} = [\mathrm{OH}]\left(1 + \frac{[\mathrm{Bz}]\,k_{\mathrm{Bz+OH}}(T)}{[\mathrm{Nap}]\,k_{\mathrm{Nap+OH}}(T)}\right) \tag{10}$$

where $k_{\mathrm{Bz+OH}}$ is 3.8×10^{-12} [cm^3 molecule^{-1} s^{-1}] $\exp\left(\frac{-2.83\,\mathrm{kJ\ mol^{-1}}}{RT}\right)$ from Baulch et al. 1992.

S3.3 Estimation of atmospheric aging from predicted OH

The atmospheric ageing estimation is based on averaged values from experiments 1-8. These calculations within this subsection were only used to estimate atmospheric ageing and were not used for further analysis. The amount of H_2O_2 dispersed into the chamber is described by Equations (11)-(13). The mass of H_2O_2 ($m_{H_2O_2}$) was calculated from the injected volume $V_{H_2O_2}$ (1 mL), the density $\rho_{H_2O_2}$ (1.450 g/m^3 at 20 °C), and the solution mass fraction (wt%), which was 50%.

$$m_{H_2O_2}[g] = V_{H_2O_2} \cdot \rho_{H_2O_2} \cdot wt\% \tag{11}$$

The amount of substance of H_2O_2 ($n_{H_2O_2}$) was estimated from the mass and molar mass of H_2O_2:

$$n_{H_2O_2}[mol] = m_{H_2O_2}/M_{H_2O_2} \tag{12}$$

The number concentration of H_2O_2 ($N_{H_2O_2}$) is then obtained by multiplying by Avogadro's number ($N_A = 6.022 \times 10^{23}$ molecules/mol) and dividing by the chamber volume ($V_{IASC} = 27 \times 10^6$ cm^3):

$$n_{H_2O_2}[molecules/cm^3] = (n_{H_2O_2} \cdot N_A)/V_{IASC} \tag{13}$$

The predicted OH number concentration ($n_{OH,pred}$) was additionally calculated from the balance between OH production (P_{OH}) and loss (L_{OH}), as described by Equations (14)-(16).

$$P_{OH} = 2 \cdot J_{H_2O_2} \cdot n_{H_2O_2} \tag{14}$$

Where $J_{H_2O_2}$ is estimated from UVAB lamps to be $2.42 \times 10^{-5} s^{-1}$.

$$L_{OH} = n_{H_2O_2} \cdot k_{H_2O_2+OH} + n_{NO} \cdot k_{NO+OH} + n_{Nap} \cdot k_{Nap+OH} + n_{Bz} \cdot k_{Bz+OH} \tag{15}$$

Where the OH + H_2O_2 reaction rate was $k_{H_2O_2+OH} = 1.70 \times 10^{-12}$ [cm^{-3} molecule^{-1} s^{-1}] Atkinson et al. (2004).
where $k_{\mathrm{Bz+OH}}$ is 3.8×10^{-12} [cm^3 molecule^{-1} s^{-1}] $\exp\left(\frac{-2.83\,\mathrm{kJ\ mol^{-1}}}{RT}\right)$ from Baulch et al. 1992. where $k_{\mathrm{Nap+OH}}$ is 1.05×10^{-12} [cm^3 molecule^{-1} s^{-1}] $\exp\left(\frac{7.50\,(\pm 2.03\,\mathrm{kJ\ mol^{-1}})}{RT}\right)$ from Atkinson 1986.

$$n_{OH,pred} = P_{OH}/L_{OH} \quad (16)$$

$$t_{aging} = t_{duration} \cdot \frac{n_{OH,pred}}{n_{OH,atm}} \quad (17)$$

The potential atmospheric ageing time (t_{aging}) was estimated using Equation 3.17 by comparing $n_{OH,pred}$ with an average atmospheric OH concentration ($n_{OH,atm} = 2.3 \times 10^6$ molecules/cm^3 (Heard and Pilling, 2003)). For IASC (batch mode), $t_{duration}$ depended on the experiment length, and the atmospheric aging is calculated for 5 min, 10 min, 20 min, 30 min, 60 min and 120 min to be 0.9 (0.01) hr, 1.9 (0.02) hr, 3.8 (0.03) hr, 5.6 (0.05) hr, 11.3 (0.1) hr and 22.4 (0.2) hr, respectively.

S3.4 Empirical OH estimation, and the calculation of the OH production rate

For the experiments conducted in positive mode, OH concentrations were estimated from the measured naphthalene decay. For these experiments, x_{Nap} was obtained from the ToF-CIMS signal, x_{Bz}, and the amount of H_2O_2 was determined from the injected volumes, and RH and NO were obtained from the chamber monitors. NO was included as a predictor because it can influence OH concentrations through reactions with peroxy radicals, particularly by converting HO_2 to OH. Experiments 1–3, 6, and 10 contained added NO, whereas Experiments 4, 5, and experiment 9 used iodide CIMS according to Table S1. Experiments 7 and 8 contained benzene only. The mean NO concentration measured before the UV lamps were switched on was used in the model. Because all experiments were performed with H_2O_2 and naphthalene, this case was used as the reference. The model results are presented in Figure S20, and the fitted equation is

$$[\text{OH}] \times 10^6 \,\text{molecules cm}^{-3} = a_0 + a_1 \cdot x_{Nap} + a_2 \cdot x_{bz} + a_3 \cdot V_{H_2O_2} + a_4 \cdot RH + a_5 \cdot x_{NO} \quad (18)$$

where a_0 = 16.3, $a_1 = -1.8 \times 10^{-7}$ per 1 ppbv change in naphthalene (relative to 30 ppbv), $a_2 = -1.8 \times 10^{-8}$ per 1 ppbv benzene, $a_3 = 3.2 \times 10^{-6}$ per 1 mL change in H_2O_2 (relative to 1 mL), $a_4 = 0.04 \times 10^{-5}$ per 1% RH (relative to 4% RH), and a_5 = 0.19 per 1 ppbv NO.

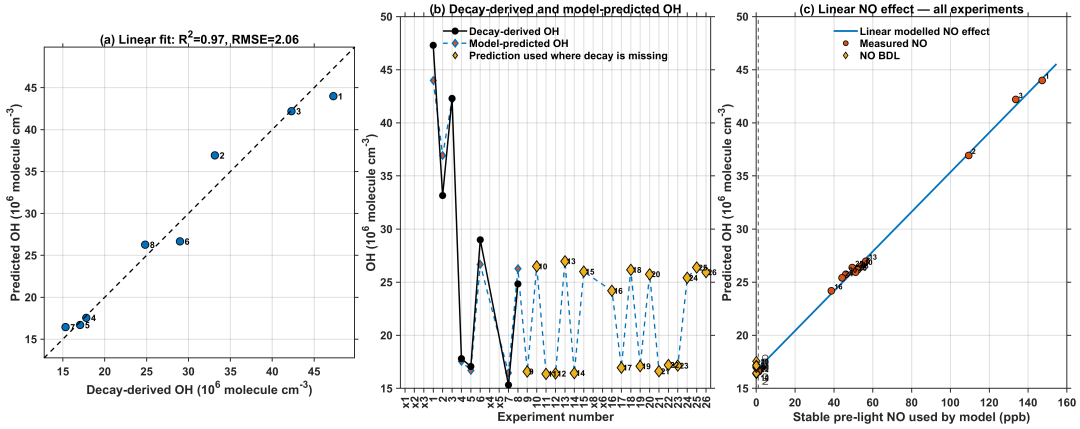


Figure S20. Empirical OH model trained on Experiments 1-8 (a), used to predict OH concentrations for the remaining experiments (b). NO was found to be an important predictor, accelerating OH formation (c).

S3.5 Production rate of OH, r_{OH}

The OH production rate was estimated from the OH concentrations (derived from naphthalene decay or predicted by the empirical model; Figure S20) and the effective OH loss rate. Assuming that naphthalene decay is driven by OH-initiated chemistry,

$$p_{\mathrm{OH}} = L_{\mathrm{OH}} = [\mathrm{OH}]\, k'_{\mathrm{OH}} \tag{19}$$

where the effective first-order OH loss rate is

$$k'_{\mathrm{OH}} = [\mathrm{Nap}]\, k_{\mathrm{Nap+OH}} + [\mathrm{Bz}]\, k_{\mathrm{Bz+OH}} + [\mathrm{SO_2}]\, k_{\mathrm{SO_2+OH}} + [\mathrm{NO_2}]\, k_{\mathrm{NO_2+OH}}. \tag{20}$$

Rate constants were taken from the literature: $k_{\mathrm{Nap+OH}}$ (Atkinson, 1986), $k_{\mathrm{Bz+OH}}$ (Baulch et al., 1992), $k_{\mathrm{SO_2+OH}}$ (Atkinson et al., 2004), and $k_{\mathrm{NO_2+OH}}$ (Atkinson et al., 1997).

The calculated (r_{OH}) for each reaction mixture is presented in Figure S21 together with the SOA-to-naphthalene mass ratio (m_{SOA}/m_{Nap}).

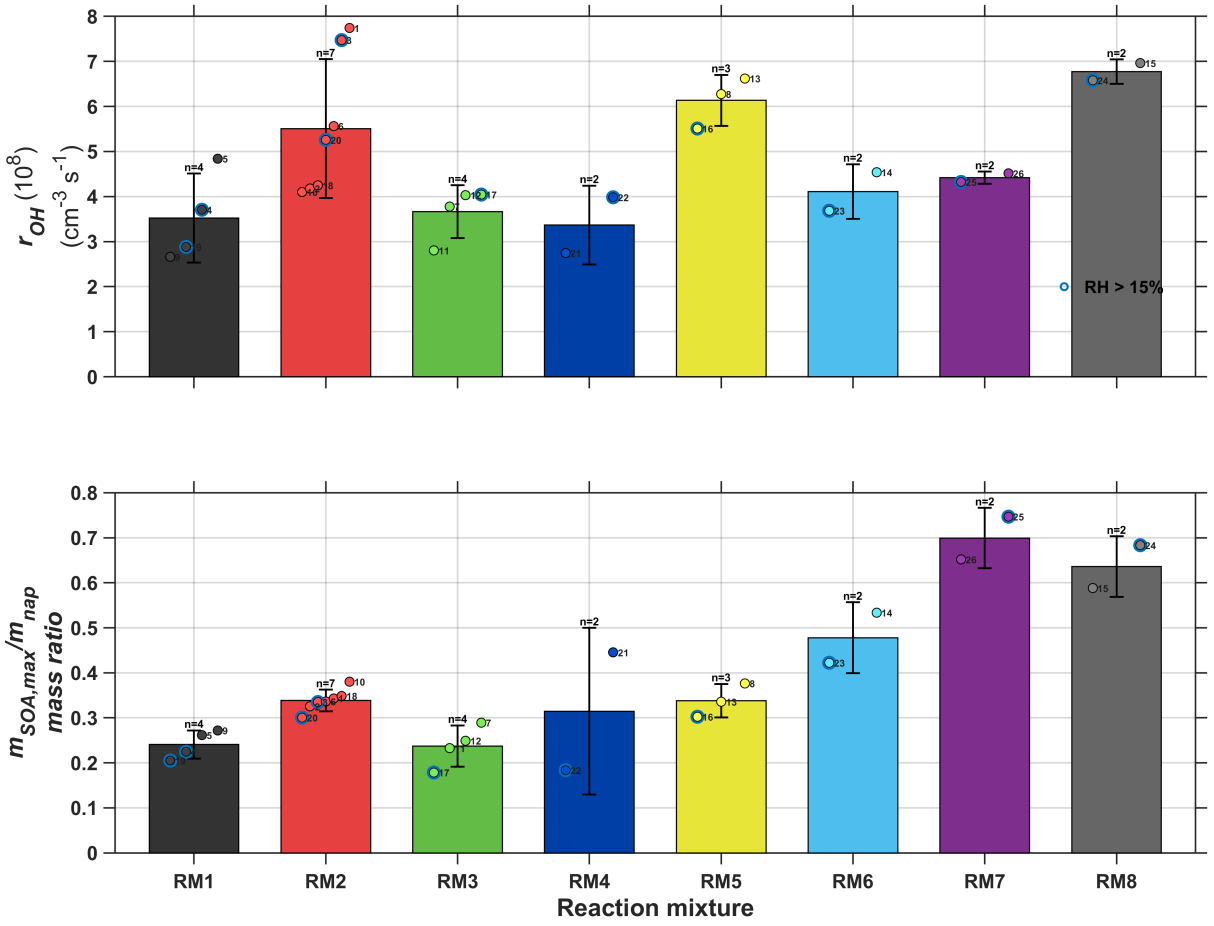


Figure S21. r_{OH} (upper panel) and m_{SOA}/m_{Nap} (lower panel) for each reaction mixture (RM). The experiments with RH >15% are circled with blue.

S4 Time-series for each experiment and overview tables

Figures S22-S47 show time series for all experiments included in this study. Tables S1-S3 summarise the initial experimental conditions (Table S1), estimated OH concentrations and production rates (Table S2), and aerosol physical properties for each experiment (Table S3).

S4.1 Experiment time-series

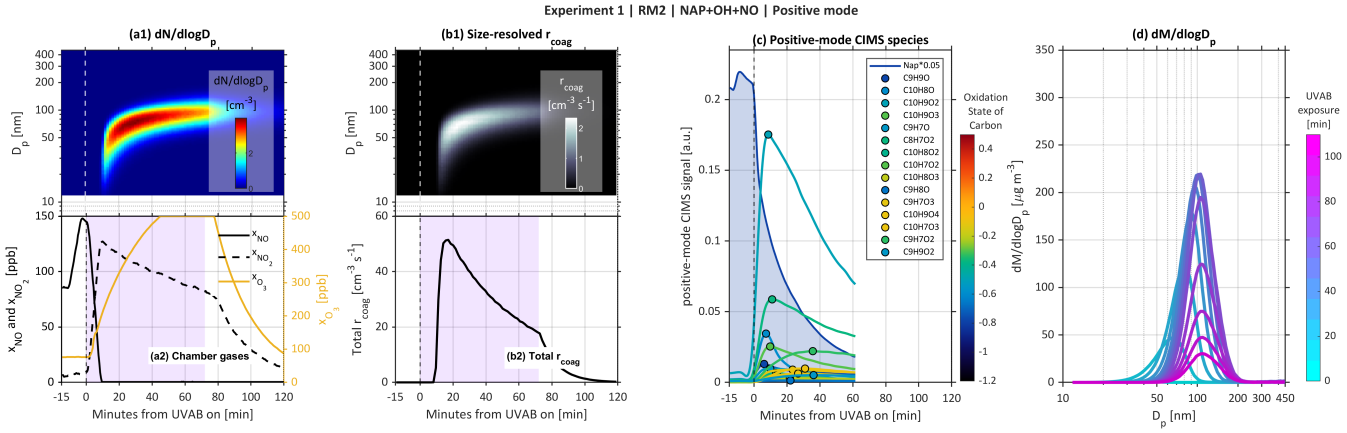


Figure S22. Time evolution of (a1) the particle number size distribution, (a2) gas-phase concentrations measured by the gas analyzers, (b1) the size-resolved coagulation rate, (b2) the total coagulation rate, and (c) selected species measured by ToF-CIMS, shown relative to the time at which the UV-A/B lamps in the chamber were switched on. Panel (d) shows the evolution of the particle mass size distribution with increasing UV-A/B exposure time. Data are shown for Experiment 1 (RM2), in which the ToF-CIMS was operated in positive mode.

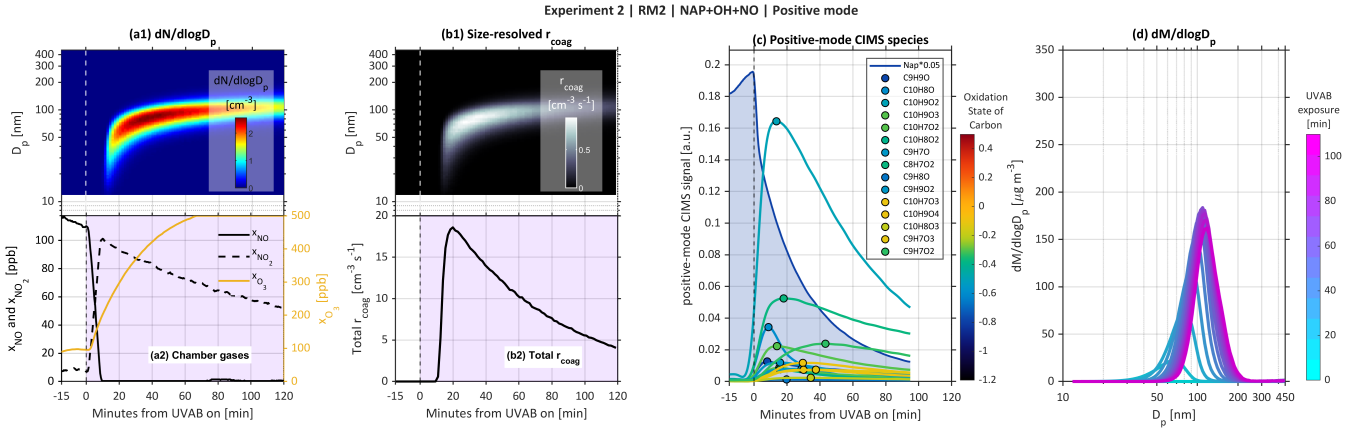


Figure S23. Time evolution of (a1) the particle number size distribution, (a2) gas-phase concentrations measured by the gas analyzers, (b1) the size-resolved coagulation rate, (b2) the total coagulation rate, and (c) selected species measured by ToF-CIMS, shown relative to the time at which the UV-A/B lamps in the chamber were switched on. Panel (d) shows the evolution of the particle mass size distribution with increasing UV-A/B exposure time. Data are shown for Experiment 2 (RM2), in which the ToF-CIMS was operated in positive mode.

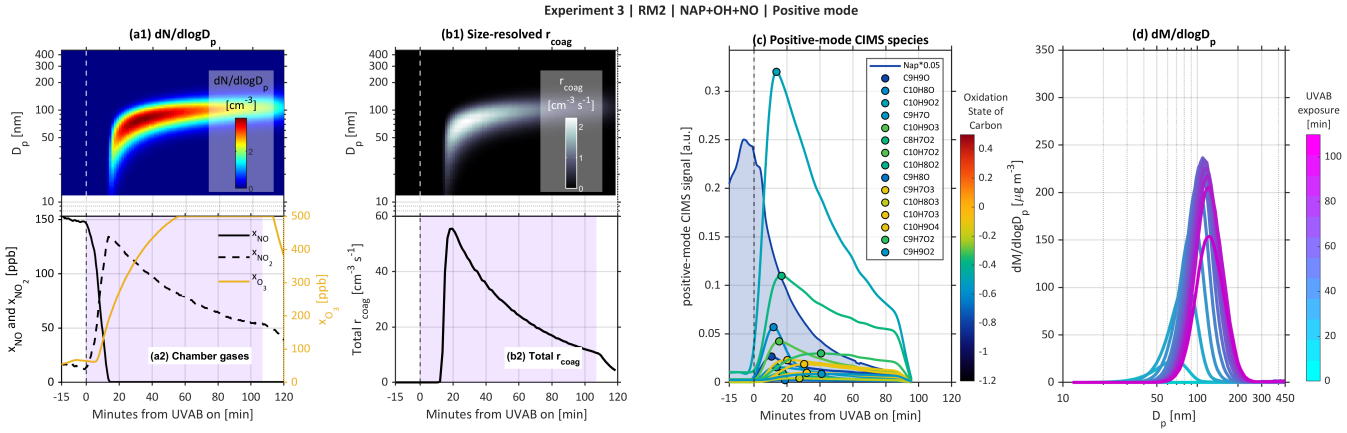


Figure S24. Time evolution of (a1) the particle number size distribution, (a2) gas-phase concentrations measured by the gas analyzers, (b1) the size-resolved coagulation rate, (b2) the total coagulation rate, and (c) selected species measured by ToF-CIMS, shown relative to the time at which the UV-A/B lamps in the chamber were switched on. Panel (d) shows the evolution of the particle mass size distribution with increasing UV-A/B exposure time. Data are shown for Experiment 3 (RM2), in which the ToF-CIMS was operated in positive mode.

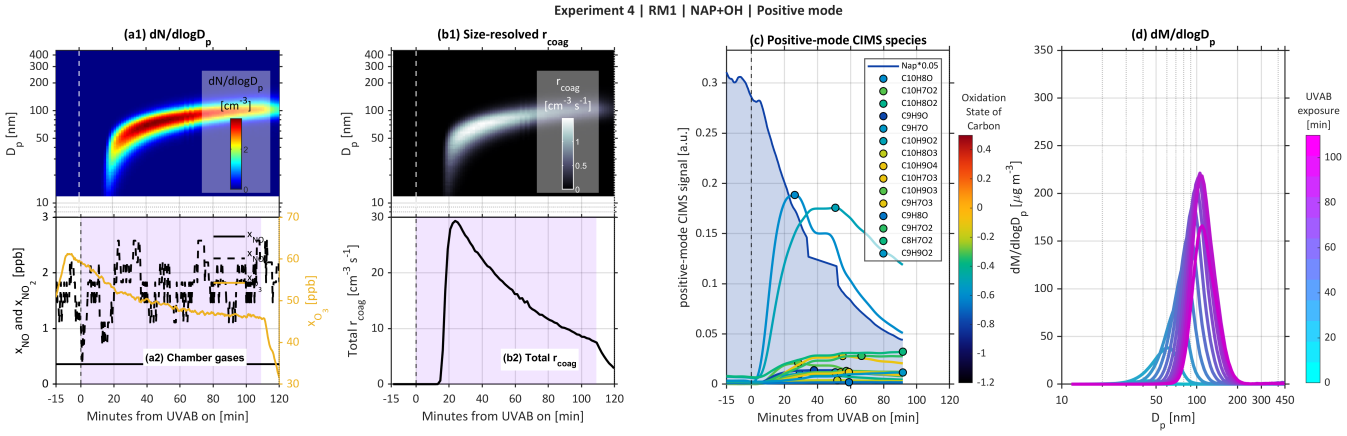


Figure S25. Time evolution of (a1) the particle number size distribution, (a2) gas-phase concentrations measured by the gas analyzers, (b1) the size-resolved coagulation rate, (b2) the total coagulation rate, and (c) selected species measured by ToF-CIMS, shown relative to the time at which the UV-A/B lamps in the chamber were switched on. Panel (d) shows the evolution of the particle mass size distribution with increasing UV-A/B exposure time. Data are shown for Experiment 4 (RM1), in which the ToF-CIMS was operated in positive mode.

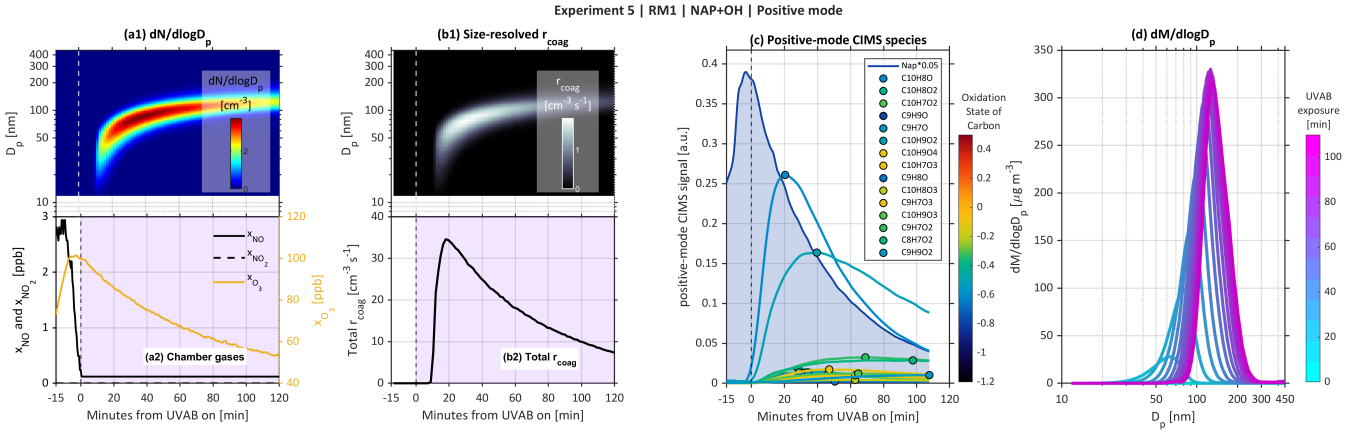


Figure S26. Time evolution of (a1) the particle number size distribution, (a2) gas-phase concentrations measured by the gas analyzers, (b1) the size-resolved coagulation rate, (b2) the total coagulation rate, and (c) selected species measured by ToF-CIMS, shown relative to the time at which the UV-A/B lamps in the chamber were switched on. Panel (d) shows the evolution of the particle mass size distribution with increasing UV-A/B exposure time. Data are shown for Experiment 5 (RM1), in which the ToF-CIMS was operated in positive mode.

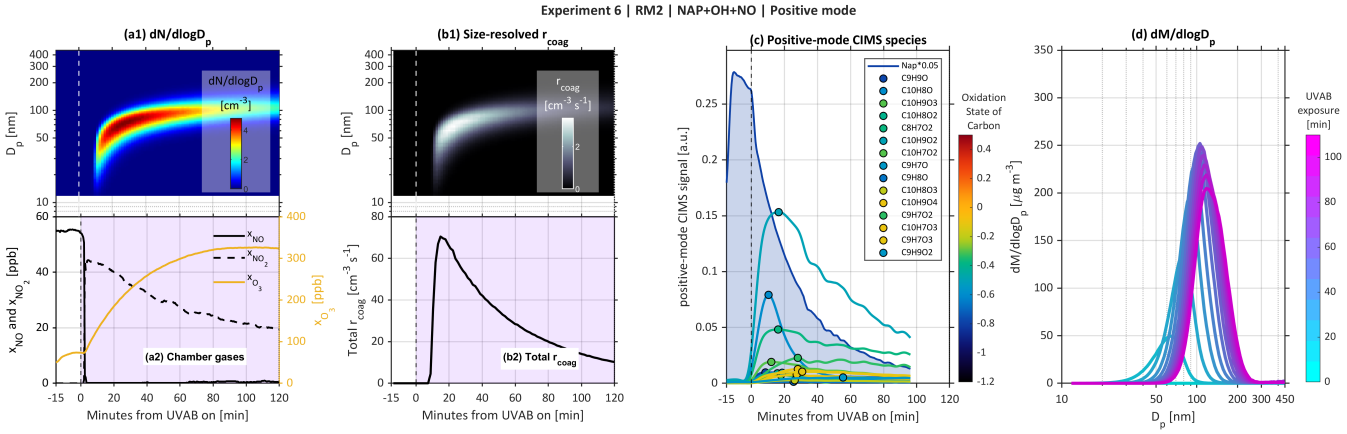


Figure S27. Time evolution of (a1) the particle number size distribution, (a2) gas-phase concentrations measured by the gas analyzers, (b1) the size-resolved coagulation rate, (b2) the total coagulation rate, and (c) selected species measured by ToF-CIMS, shown relative to the time at which the UV-A/B lamps in the chamber were switched on. Panel (d) shows the evolution of the particle mass size distribution with increasing UV-A/B exposure time. Data are shown for Experiment 6 (RM2), in which the ToF-CIMS was operated in positive mode.

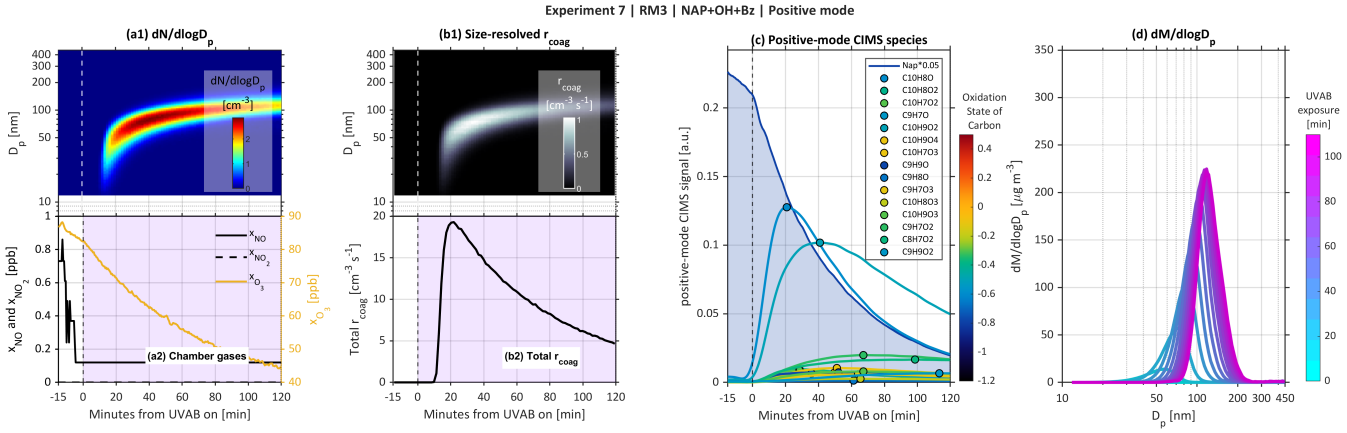


Figure S28. Time evolution of (a1) the particle number size distribution, (a2) gas-phase concentrations measured by the gas analyzers, (b1) the size-resolved coagulation rate, (b2) the total coagulation rate, and (c) selected species measured by ToF-CIMS, shown relative to the time at which the UV-A/B lamps in the chamber were switched on. Panel (d) shows the evolution of the particle mass size distribution with increasing UV-A/B exposure time. Data are shown for Experiment 7 (RM3), in which the ToF-CIMS was operated in positive mode.

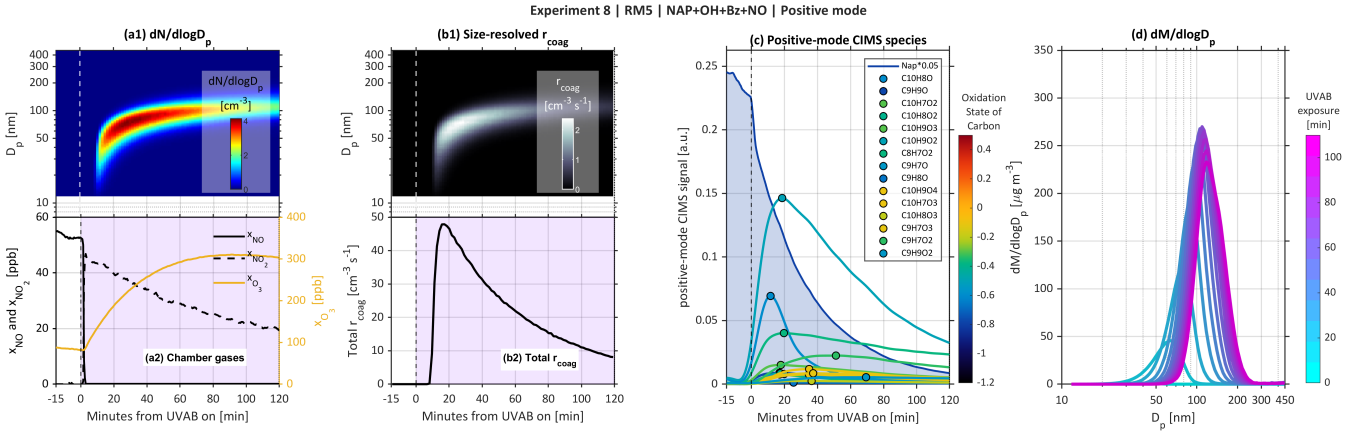


Figure S29. Time evolution of (a1) the particle number size distribution, (a2) gas-phase concentrations measured by the gas analyzers, (b1) the size-resolved coagulation rate, (b2) the total coagulation rate, and (c) selected species measured by ToF-CIMS, shown relative to the time at which the UV-A/B lamps in the chamber were switched on. Panel (d) shows the evolution of the particle mass size distribution with increasing UV-A/B exposure time. Data are shown for Experiment 9 (RM1), in which the ToF-CIMS was operated in negative mode.

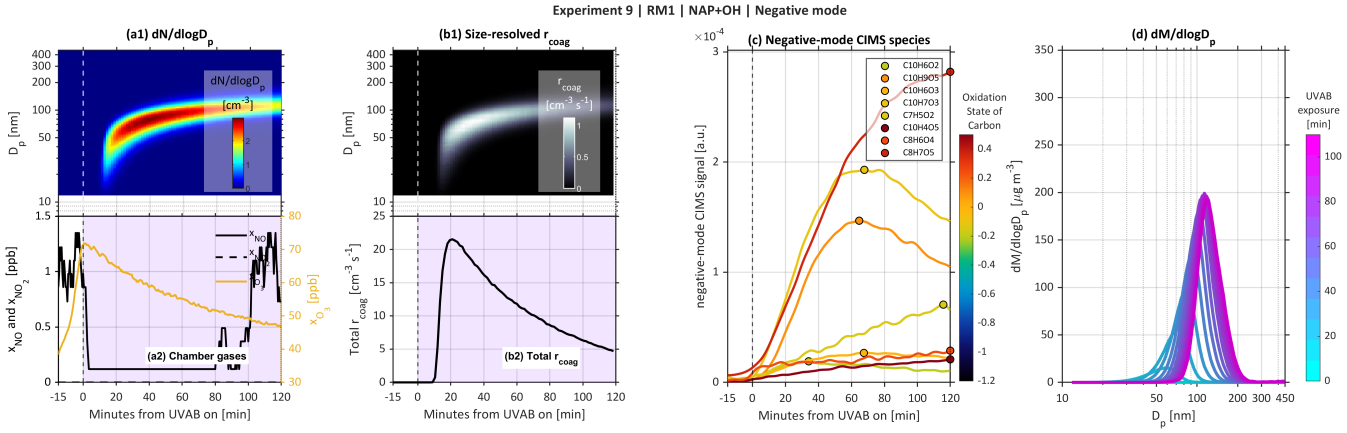


Figure S30. Time evolution of (a1) the particle number size distribution, (a2) gas-phase concentrations measured by the gas analyzers, (b1) the size-resolved coagulation rate, (b2) the total coagulation rate, and (c) selected species measured by ToF-CIMS, shown relative to the time at which the UV-A/B lamps in the chamber were switched on. Panel (d) shows the evolution of the particle mass size distribution with increasing UV-A/B exposure time. Data are shown for Experiment 10 (RM2), in which the ToF-CIMS was operated in negative mode.

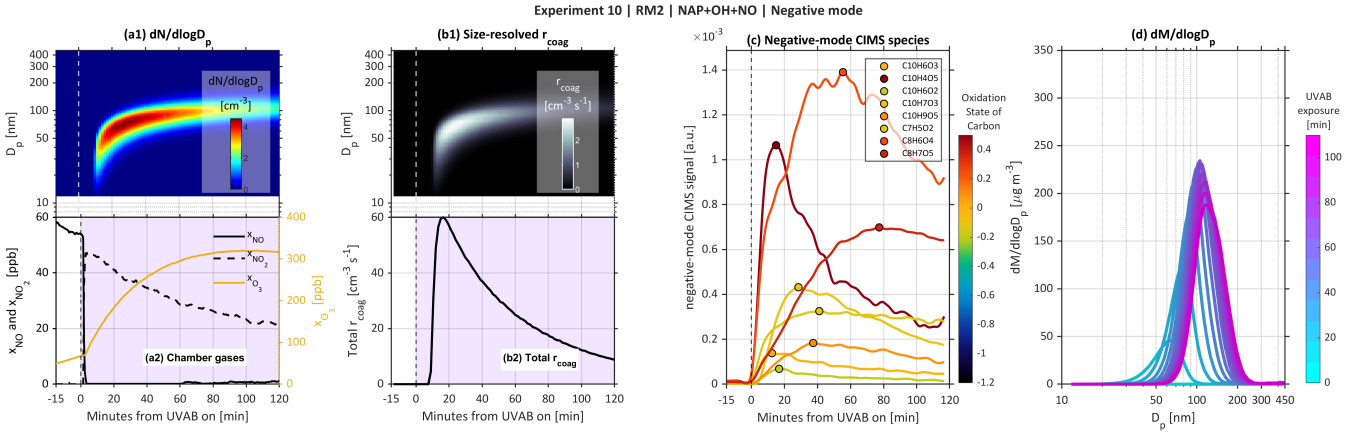


Figure S31. Time evolution of (a1) the particle number size distribution, (a2) gas-phase concentrations measured by the gas analyzers, (b1) the size-resolved coagulation rate, (b2) the total coagulation rate, and (c) selected species measured by ToF-CIMS, shown relative to the time at which the UV-A/B lamps in the chamber were switched on. Panel (d) shows the evolution of the particle mass size distribution with increasing UV-A/B exposure time. Data are shown for Experiment 11 (RM3), in which the ToF-CIMS was operated in negative mode.

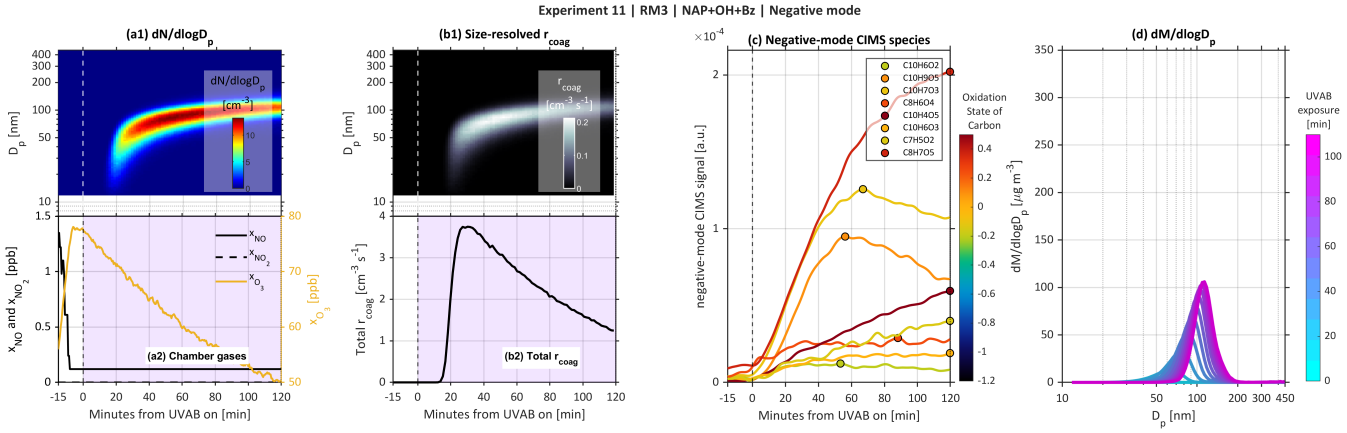


Figure S32. Time evolution of (a1) the particle number size distribution, (a2) gas-phase concentrations measured by the gas analyzers, (b1) the size-resolved coagulation rate, (b2) the total coagulation rate, and (c) selected species measured by ToF-CIMS, shown relative to the time at which the UV-A/B lamps in the chamber were switched on. Panel (d) shows the evolution of the particle mass size distribution with increasing UV-A/B exposure time. Data are shown for Experiment 12 (RM3), in which the ToF-CIMS was operated in negative mode.

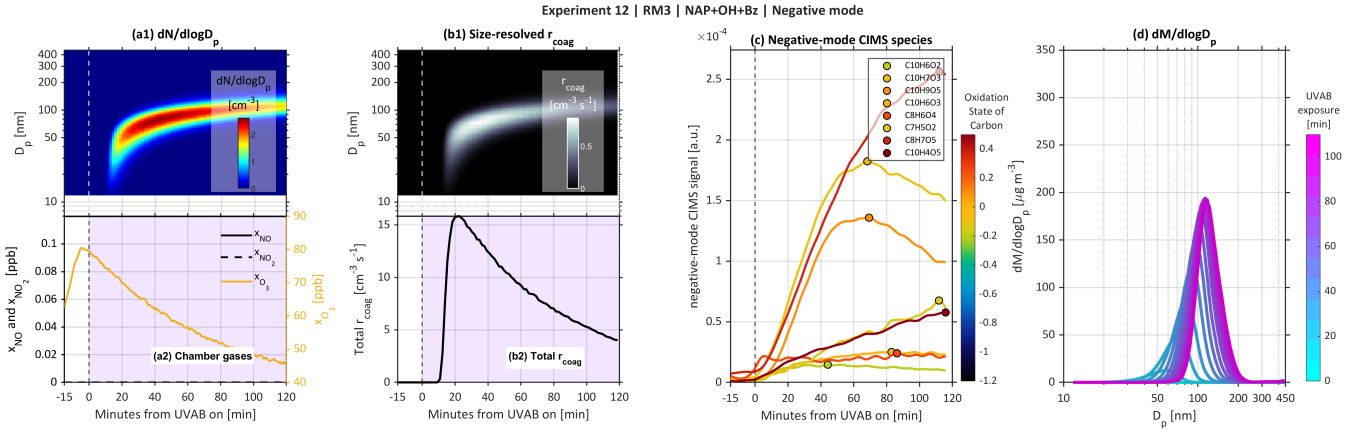


Figure S33. Time evolution of (a1) the particle number size distribution, (a2) gas-phase concentrations measured by the gas analyzers, (b1) the size-resolved coagulation rate, (b2) the total coagulation rate, and (c) selected species measured by ToF-CIMS, shown relative to the time at which the UV-A/B lamps in the chamber were switched on. Panel (d) shows the evolution of the particle mass size distribution with increasing UV-A/B exposure time. Data are shown for Experiment 13 (RM5), in which the ToF-CIMS was operated in negative mode.

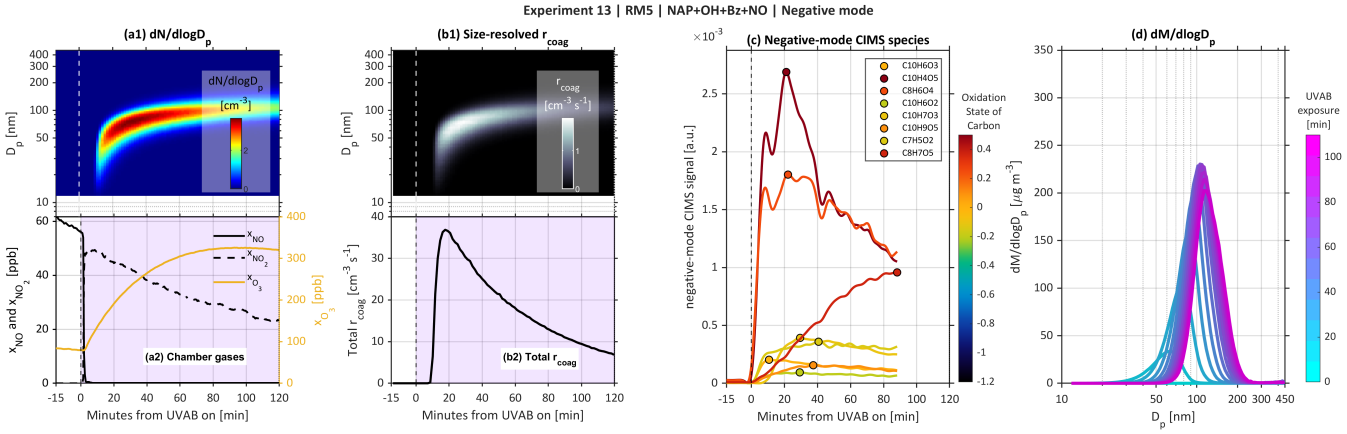


Figure S34. Time evolution of (a1) the particle number size distribution, (a2) gas-phase concentrations measured by the gas analyzers, (b1) the size-resolved coagulation rate, (b2) the total coagulation rate, and (c) selected species measured by ToF-CIMS, shown relative to the time at which the UV-A/B lamps in the chamber were switched on. Panel (d) shows the evolution of the particle mass size distribution with increasing UV-A/B exposure time. Data are shown for Experiment 14 (RM6), in which the ToF-CIMS was operated in negative mode.

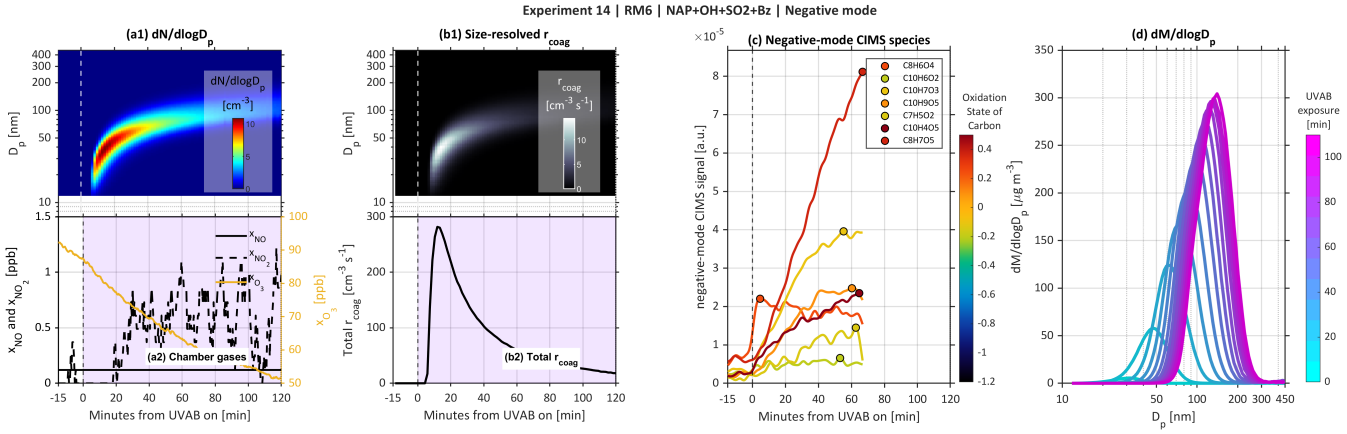


Figure S35. Time evolution of (a1) the particle number size distribution, (a2) gas-phase concentrations measured by the gas analyzers, (b1) the size-resolved coagulation rate, (b2) the total coagulation rate, and (c) selected species measured by ToF-CIMS, shown relative to the time at which the UV-A/B lamps in the chamber were switched on. Panel (d) shows the evolution of the particle mass size distribution with increasing UV-A/B exposure time. Data are shown for Experiment 15 (RM8), in which the ToF-CIMS was operated in negative mode.

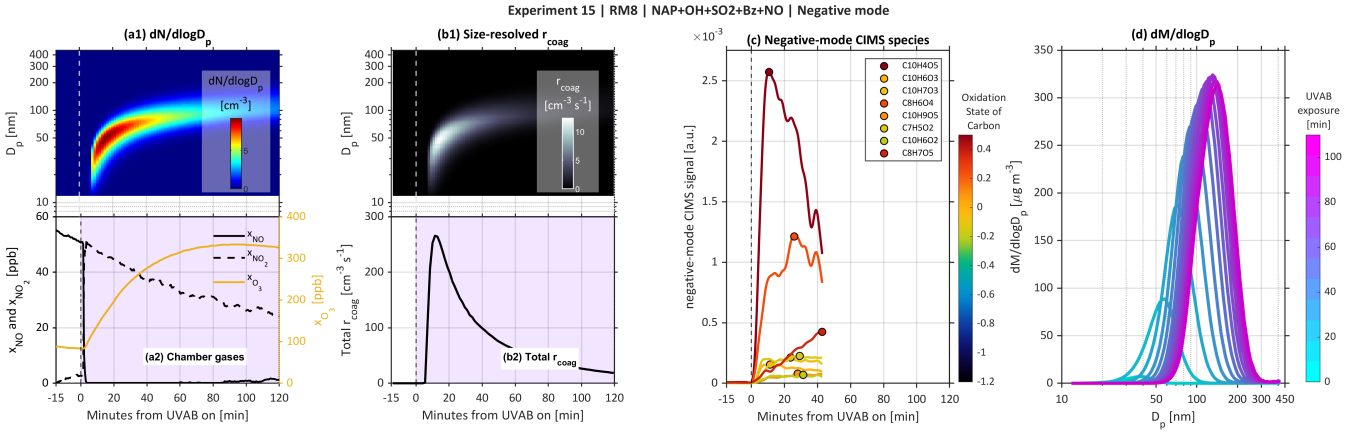


Figure S36. Time evolution of (a1) the particle number size distribution, (a2) gas-phase concentrations measured by the gas analyzers, (b1) the size-resolved coagulation rate, (b2) the total coagulation rate, and (c) selected species measured by ToF-CIMS, shown relative to the time at which the UV-A/B lamps in the chamber were switched on. Panel (d) shows the evolution of the particle mass size distribution with increasing UV-A/B exposure time. Data are shown for Experiment 16 (RM2), in which the ToF-CIMS was operated in negative mode.

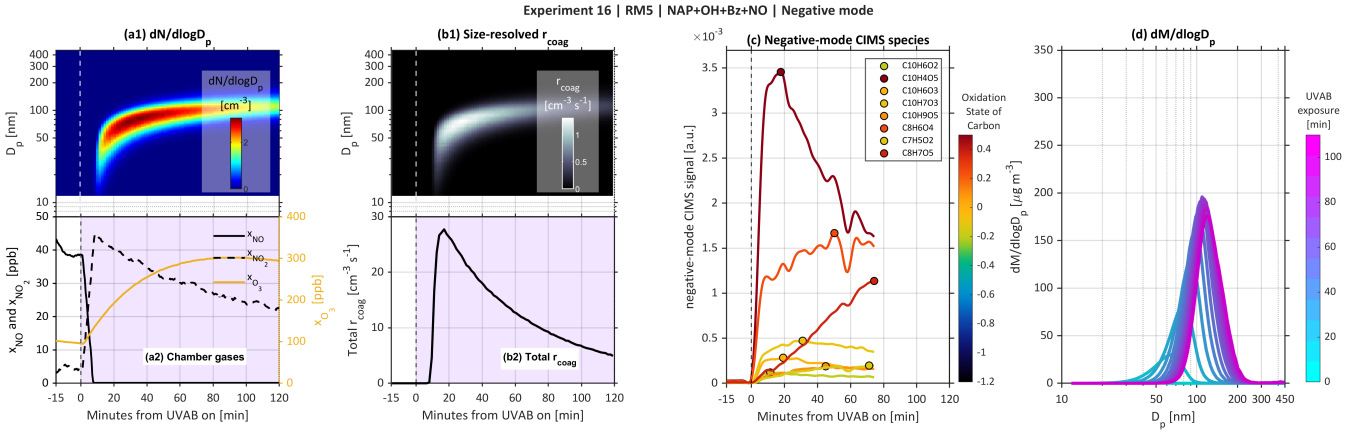


Figure S37. Time evolution of (a1) the particle number size distribution, (a2) gas-phase concentrations measured by the gas analyzers, (b1) the size-resolved coagulation rate, (b2) the total coagulation rate, and (c) selected species measured by ToF-CIMS, shown relative to the time at which the UV-A/B lamps in the chamber were switched on. Panel (d) shows the evolution of the particle mass size distribution with increasing UV-A/B exposure time. Data are shown for Experiment 17 (RM3), in which the ToF-CIMS was operated in negative mode.

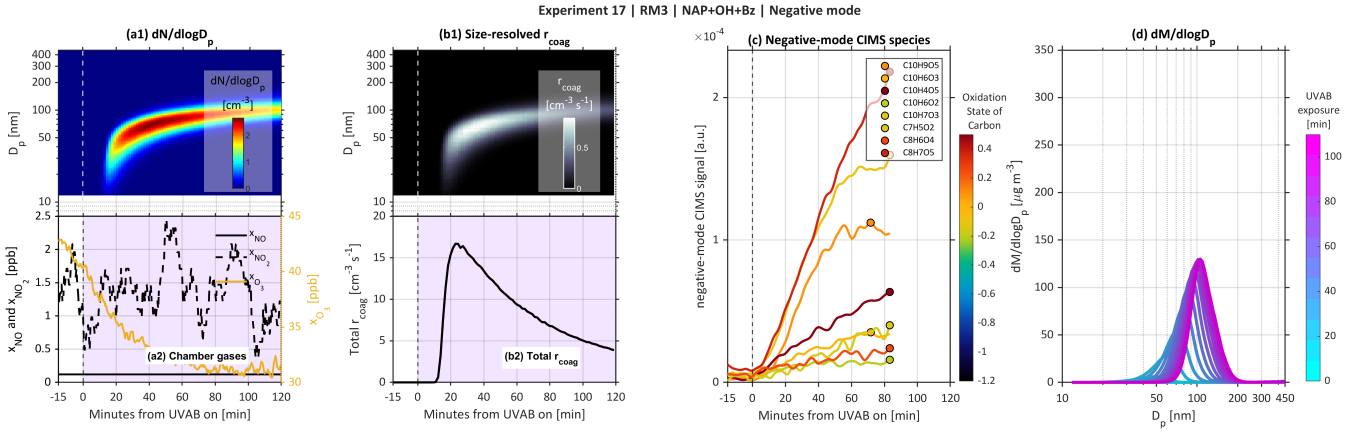


Figure S38. Time evolution of (a1) the particle number size distribution, (a2) gas-phase concentrations measured by the gas analyzers, (b1) the size-resolved coagulation rate, (b2) the total coagulation rate, and (c) selected species measured by ToF-CIMS, shown relative to the time at which the UV-A/B lamps in the chamber were switched on. Panel (d) shows the evolution of the particle mass size distribution with increasing UV-A/B exposure time. Data are shown for Experiment 18 (RM2), in which the ToF-CIMS was operated in negative mode.

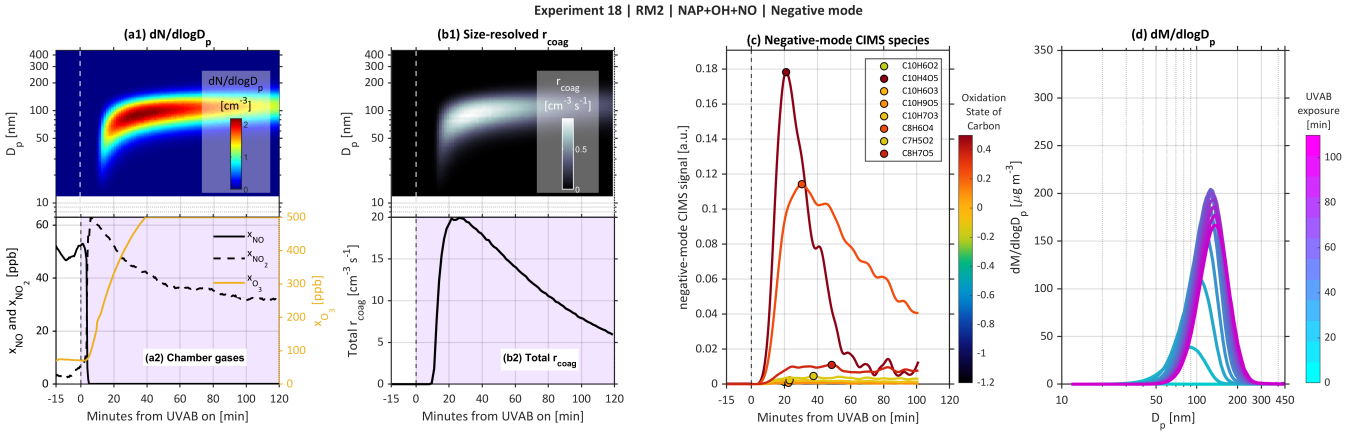


Figure S39. Time evolution of (a1) the particle number size distribution, (a2) gas-phase concentrations measured by the gas analyzers, (b1) the size-resolved coagulation rate, (b2) the total coagulation rate, and (c) selected species measured by ToF-CIMS, shown relative to the time at which the UV-A/B lamps in the chamber were switched on. Panel (d) shows the evolution of the particle mass size distribution with increasing UV-A/B exposure time. Data are shown for Experiment 19 (RM2), in which the ToF-CIMS was operated in negative mode.

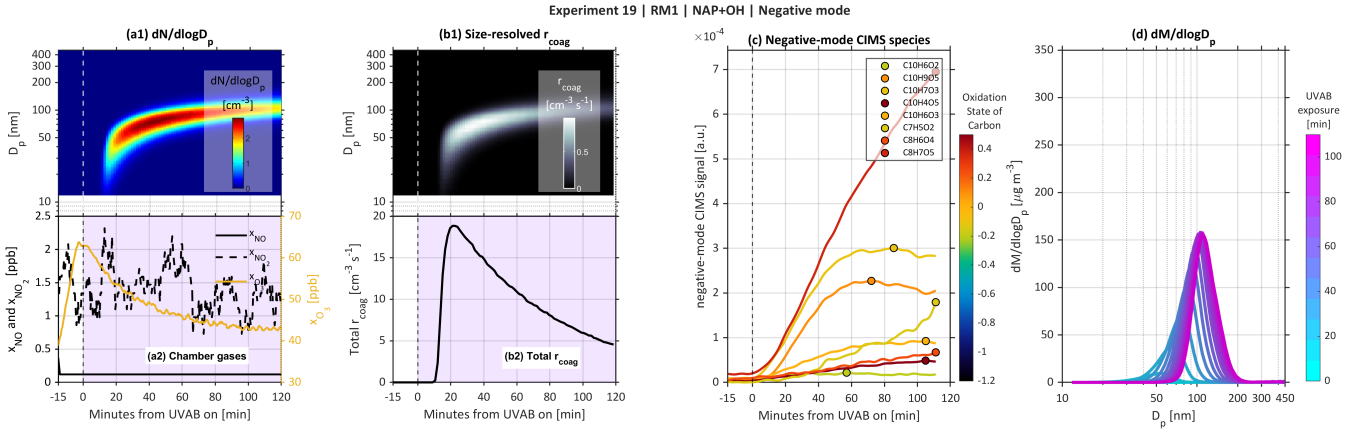


Figure S40. Time evolution of (a1) the particle number size distribution, (a2) gas-phase concentrations measured by the gas analyzers, (b1) the size-resolved coagulation rate, (b2) the total coagulation rate, and (c) selected species measured by ToF-CIMS, shown relative to the time at which the UV-A/B lamps in the chamber were switched on. Panel (d) shows the evolution of the particle mass size distribution with increasing UV-A/B exposure time. Data are shown for Experiment 20 (RM1), in which the ToF-CIMS was operated in negative mode.

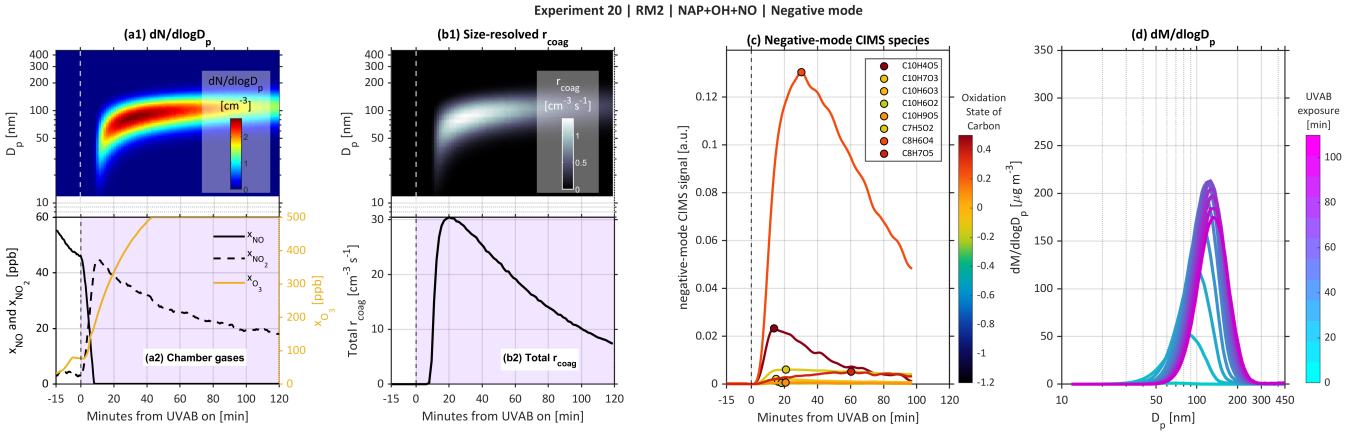


Figure S41. Time evolution of (a1) the particle number size distribution, (a2) gas-phase concentrations measured by the gas analyzers, (b1) the size-resolved coagulation rate, (b2) the total coagulation rate, and (c) selected species measured by ToF-CIMS, shown relative to the time at which the UV-A/B lamps in the chamber were switched on. Panel (d) shows the evolution of the particle mass size distribution with increasing UV-A/B exposure time. Data are shown for Experiment 21 (RM2), in which the ToF-CIMS was operated in negative mode.

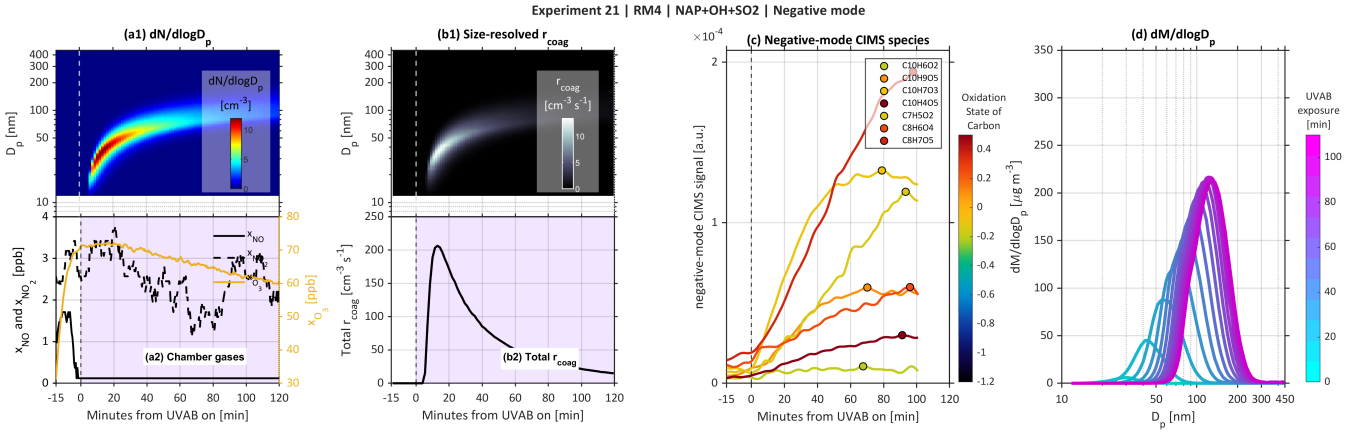


Figure S42. Time evolution of (a1) the particle number size distribution, (a2) gas-phase concentrations measured by the gas analyzers, (b1) the size-resolved coagulation rate, (b2) the total coagulation rate, and (c) selected species measured by ToF-CIMS, shown relative to the time at which the UV-A/B lamps in the chamber were switched on. Panel (d) shows the evolution of the particle mass size distribution with increasing UV-A/B exposure time. Data are shown for Experiment 22 (RM4), in which the ToF-CIMS was operated in negative mode.

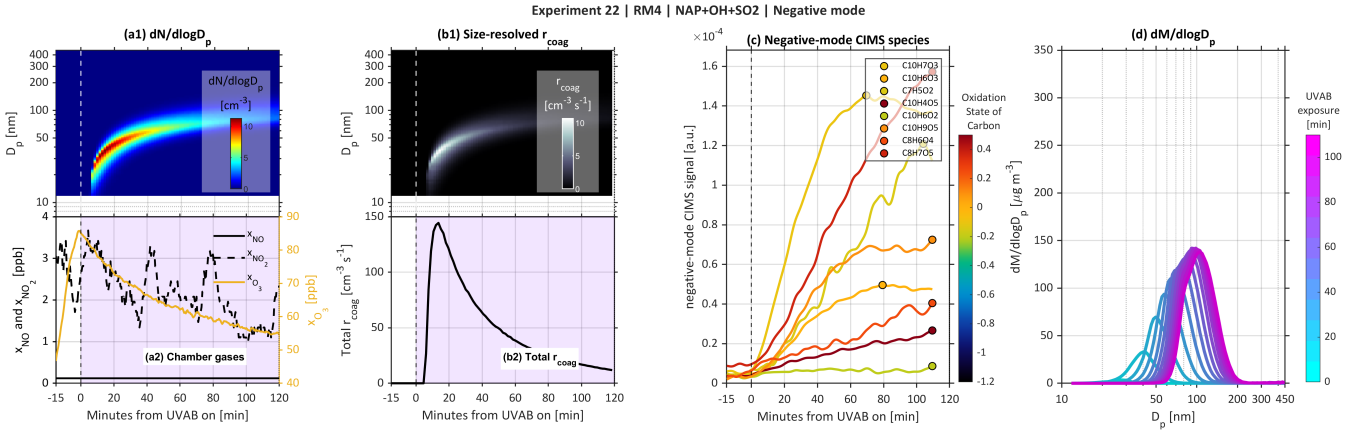


Figure S43. Time evolution of (a1) the particle number size distribution, (a2) gas-phase concentrations measured by the gas analyzers, (b1) the size-resolved coagulation rate, (b2) the total coagulation rate, and (c) selected species measured by ToF-CIMS, shown relative to the time at which the UV-A/B lamps in the chamber were switched on. Panel (d) shows the evolution of the particle mass size distribution with increasing UV-A/B exposure time. Data are shown for Experiment 23 (RM4), in which the ToF-CIMS was operated in negative mode.

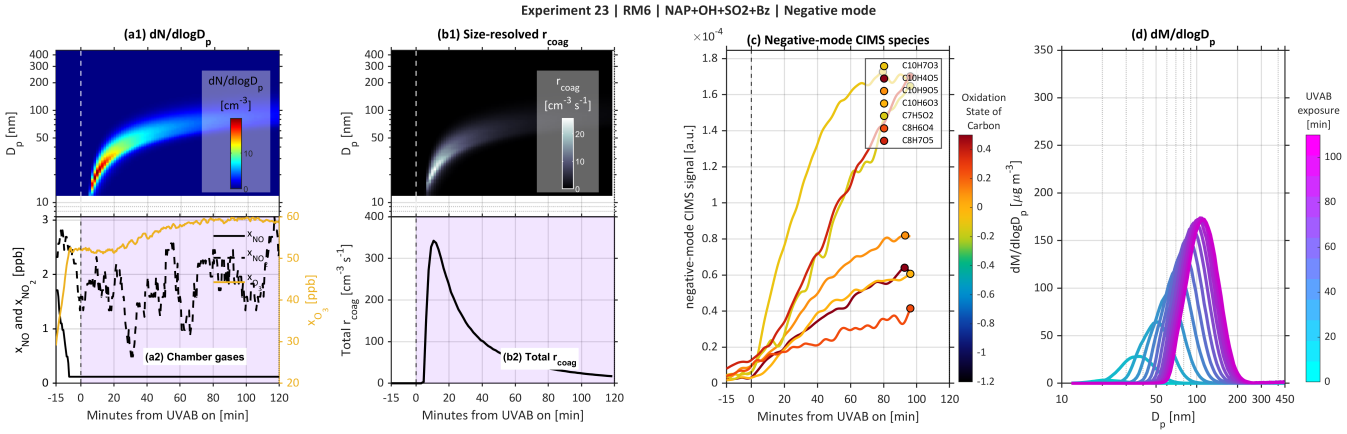


Figure S44. Time evolution of (a1) the particle number size distribution, (a2) gas-phase concentrations measured by the gas analyzers, (b1) the size-resolved coagulation rate, (b2) the total coagulation rate, and (c) selected species measured by ToF-CIMS, shown relative to the time at which the UV-A/B lamps in the chamber were switched on. Panel (d) shows the evolution of the particle mass size distribution with increasing UV-A/B exposure time. Data are shown for Experiment 24 (RM6), in which the ToF-CIMS was operated in negative mode.

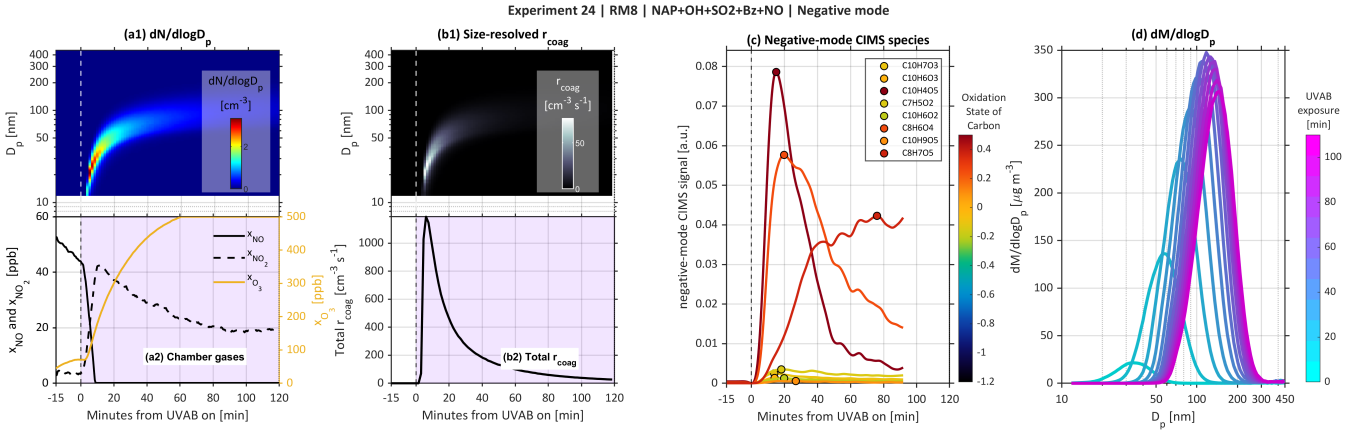


Figure S45. Time evolution of (a1) the particle number size distribution, (a2) gas-phase concentrations measured by the gas analyzers, (b1) the size-resolved coagulation rate, (b2) the total coagulation rate, and (c) selected species measured by ToF-CIMS, shown relative to the time at which the UV-A/B lamps in the chamber were switched on. Panel (d) shows the evolution of the particle mass size distribution with increasing UV-A/B exposure time. Data are shown for Experiment 25 (RM8), in which the ToF-CIMS was operated in negative mode.

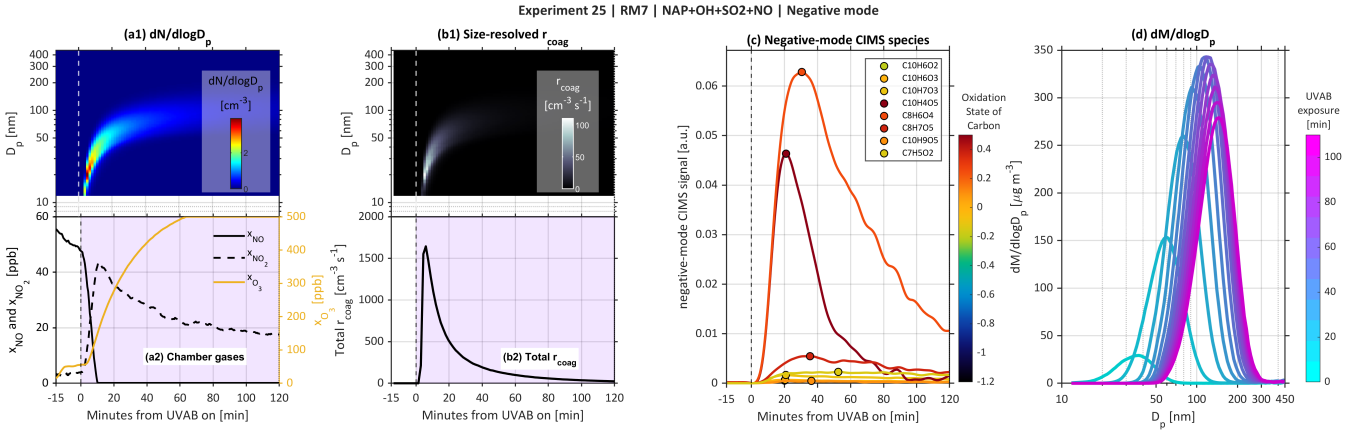


Figure S46. Time evolution of (a1) the particle number size distribution, (a2) gas-phase concentrations measured by the gas analyzers, (b1) the size-resolved coagulation rate, (b2) the total coagulation rate, and (c) selected species measured by ToF-CIMS, shown relative to the time at which the UV-A/B lamps in the chamber were switched on. Panel (d) shows the evolution of the particle mass size distribution with increasing UV-A/B exposure time. Data are shown for Experiment 26 (RM7), in which the ToF-CIMS was operated in negative mode.

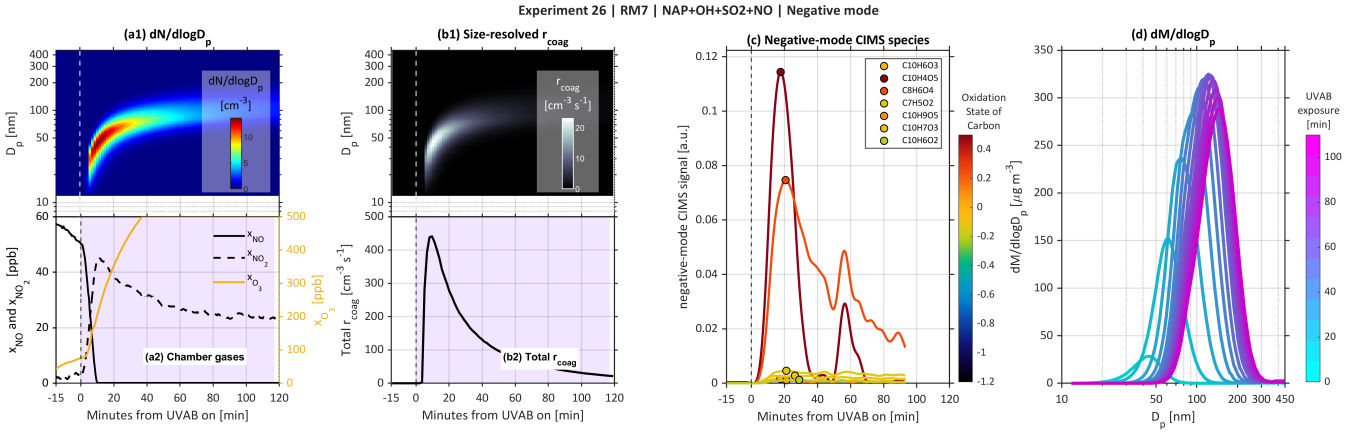


Figure S47. Time evolution of (a1) the particle number size distribution, (a2) gas-phase concentrations measured by the gas analyzers, (b1) the size-resolved coagulation rate, (b2) the total coagulation rate, and (c) selected species measured by ToF-CIMS, shown relative to the time at which the UV-A/B lamps in the chamber were switched on. Panel (d) shows the evolution of the particle mass size distribution with increasing UV-A/B exposure time. Data are shown for Experiment 26 (RM7), in which the ToF-CIMS was operated in negative mode.

Table S1. Overview table of the initial conditions measured 15 min before the UVAB lamps were turned on, with values measured 1 h after UVAB illumination began indicated by "#". BDL: below detection limit.

RM	Exp nr.	CIMS mode	x_{nap} (ppbv)	x_{bz} (ppbv)	x_{NO} (ppbv)	x_{NO2} (ppbv)	x_{SO2} (ppbv)	RH$^{\#}$ (%)	T$^{\#}$ (°C)	RH$_{int}$ (%)	T$_{int}$ (°C)
RM2	1	+	28.9	n/a	147.2	8.1	n/a	5.3	21.4	5.2	19.0
RM2	2	+	22.3	n/a	109.4	8.4	n/a	5.7	21.4	5.1	18.8
RM2	3	+	31.3	n/a	133.7	35.4	n/a	24.1	21.5	24.1	18.9
RM1	4	+	37.2	n/a	BDL	1.1	n/a	31.3	21.4	31.3	18.8
RM1	5	+	50.8	n/a	1.5	BDL	n/a	3.4	21.5	2.5	19.2
RM2	6	+	34.3	n/a	55.1	BDL	n/a	2.8	21.5	2.0	19.1
RM3	7	+	29.9	120.1	BDL	BDL	n/a	3.9	21.4	3.3	18.9
RM5	8	+	31.0	120.1	52.6	BDL	n/a	4.1	21.6	3.6	19.0
RM1	9	-	28.7	n/a	1.2	BDL	n/a	1.8	21.5	1.0	19.0
RM2	10	-	27.6	n/a	54.1	BDL	n/a	2.5	21.4	1.9	19.0
RM3	11	-	15.1	120.4	BDL	BDL	n/a	2.3	21.5	1.4	19.1
RM3	12	-	29.8	120.0	BDL	BDL	n/a	2.8	21.4	2.0	18.8
RM5	13	-	39.5	120.0	56.4	BDL	n/a	3.8	21.3	3.2	18.7
RM6	14	-	34.1	120.3	BDL	BDL	18.0	3.7	21.4	3.1	18.6
RM8	15	-	32.4	120.2	51.2	2.6	18.0	3.5	21.4	3.0	18.6
RM2	16	-	26.3	119.7	38.7	4.2	n/a	16.8	21.6	16.6	19.5
RM3	17	-	28.4	119.9	BDL	1.1	n/a	16.1	21.2	16.1	18.8
RM2	18	-	28.8	n/a	52.1	5.5	n/a	3.2	21.3	2.8	18.8
RM1	19	-	30.0	n/a	BDL	1.0	n/a	20.0	21.0	19.6	19.0
RM2	20	-	36.3	n/a	46.1	2.8	n/a	21.1	21.2	20.8	18.6
RM4	21	-	28.5	n/a	1.1	2.6	18.0	3.0	21.5	2.3	18.9
RM4	22	-	40.5	n/a	BDL	2.0	18.0	23.3	21.1	22.5	18.7
RM6	23	-	22.6	119.5	BDL	1.6	18.0	21.2	21.5	20.9	19.0
RM8	24	-	30.7	120.0	44.2	3.5	18.0	21.8	21.2	21.5	18.4
RM7	25	-	28.2	n/a	49.4	3.8	18.0	21.4	21.5	21.1	19.1
RM7	26	-	30.0	n/a	51.2	3.3	18.0	2.8	21.5	2.0	19.2

Table S2. Overview table of OH concentration ans production rates, where OH_{mix} is the OH concentrations mixed and model-based. k'_{OH} is OH sinks rates summed up from equation (13).

RM	Exp nr.	OH (10^6 cm^{-3})	OH_{mix} factor	OH** (10^6 cm^{-3})	k'_{OH} (s^{-1})	r_{OH} (10^8 cm^{-3} s^{-1})
RM2	1	47.3	1.0	47.3	16.4	7.7
RM2	2	33.2	1.0	33.2	12.6	4.2
RM2	3	42.3	1.0	42.3	17.7	7.5
RM1	4	17.8	1.0	17.8	20.8	3.7
RM1	5	17.1	1.0	17.1	28.4	4.8
RM2	6	29.0	1.0	29.0	19.2	5.6
RM3	7	15.3	1.2	18.6	20.3	3.8
RM5	8	24.8	1.2	30.0	20.9	6.3
RM1	9	16.6	1.0	16.6	16.1	2.7
RM2	10	26.5	1.0	26.5	15.5	4.1
RM3	11	16.4	1.5	23.3	12.0	2.8
RM3	12	16.4	1.2	19.9	20.2	4.0
RM5	13	27.0	1.2	31.3	20.2	6.6
RM6	14	16.4	1.2	19.5	23.2	4.5
RM8	15	26.0	1.2	31.1	22.4	7.0
RM2	16	24.2	1.2	30.1	18.3	5.5
RM3	17	16.9	1.2	20.8	19.5	4.0
RM2	18	26.2	1.0	26.2	16.2	4.2
RM1	19	17.1	1.0	17.1	16.9	2.9
RM2	20	25.7	1.0	25.7	20.4	5.3
RM4	21	16.6	1.0	16.6	16.5	2.7
RM4	22	17.2	1.0	17.2	23.2	4.0
RM6	23	17.1	1.3	22.0	21.4	3.7
RM8	24	25.4	1.2	30.7	21.4	6.6
RM7	25	26.4	1.0	26.4	16.4	4.3
RM7	26	25.9	1.0	25.9	17.4	4.5

Table S3. Overview table of the maximum particle coagulation rate, particle mass concentration, and particle number concentration, including the time after UVAB illumination at which each maximum occurs.

RM	Exp nr.	r_{coag} (cm^{-3} s^{-1})	$t_{max,r}$ (min)	n_{PNC} (10^5) (cm^{-3})	$t_{max,n}$ (min)	$m_{SOA,max}$ (μg m^{-3})	$t_{max,m}$ (min)	$m_{nap,int}$ (μg m^{-3})	$m_{SOA,max}/m_{Nap,int}$
RM2	1	51.5	17.1	1.25	15.6	52.6	66.6	153.4	0.35
RM2	2	18.6	19.9	0.74	19.9	38.4	79.9	118.1	0.34
RM2	3	54.7	19.6	1.26	18.1	55.6	69.1	165.9	0.32
RM1	4	29.3	23.7	0.97	23.7	44.3	104.7	197.3	0.23
RM1	5	34.1	17.9	1.03	17.9	70.4	107.9	269.3	0.26
RM2	6	69.6	14.8	1.49	14.8	61.1	79.3	181.6	0.35
RM3	7	19.3	21.8	0.78	20.3	45.8	108.8	158.5	0.29
RM5	8	47.9	17.2	1.22	15.7	61.8	81.7	164.2	0.38
RM1	9	21.2	21.0	0.82	19.5	41.4	102.0	152.3	0.27
RM2	10	59.3	16.5	1.37	15.0	55.6	79.5	146.2	0.38
RM3	11	3.7	30.2	0.34	27.2	18.6	114.2	80.0	0.22
RM3	12	15.8	22.8	0.70	21.3	39.3	105.3	157.9	0.25
RM5	13	36.9	17.6	1.07	17.6	52.5	94.1	156.5	0.32
RM6	14	281.7	11.9	3.23	11.9	96.4	115.4	180.7	0.53
RM8	15	265.7	11.5	3.01	11.5	101.0	101.5	171.7	0.59
RM2	16	27.4	17.0	0.92	17.0	42.2	89.0	139.6	0.29
RM3	17	16.5	22.9	0.73	22.9	26.9	111.4	150.5	0.22
RM2	18	19.6	26.0	0.72	21.5	53.3	66.5	153.0	0.34
RM1	19	18.6	21.1	0.77	21.1	32.6	105.1	159.1	0.21
RM2	20	30.0	20.0	0.90	20.0	57.9	72.5	192.7	0.29
RM4	21	203.8	13.0	2.82	11.5	67.4	109.0	151.2	0.44
RM4	22	142.6	13.6	2.37	12.1	39.2	102.1	213.3	0.18
RM6	23	337.5	10.7	3.89	9.2	50.5	112.7	119.7	0.39
RM8	24	1172.5	6.1	7.10	6.1	111.3	72.1	162.8	0.69
RM7	25	1621.7	6.0	8.52	4.5	111.7	57.0	149.5	0.76
RM7	26	435.7	9.7	3.95	8.2	103.7	71.2	159.0	0.69

S5 Comparison with the literature

Figures S48-S50 compare the results from this study (denoted "polat2026napthalene") with previous chamber studies (Chan et al., 2009; Chen et al., 2016, 2018; Kleindienst et al., 2012; Shakya and Griffin, 2010). Figure S48 shows SOA formation as a function of the initial naphthalene concentration, and our results are broadly consistent with the literature. Figure S49 compares SOA formation as a function of the initial naphthalene-to-NO ratio. Figure S50 shows SOA formation as a function of initial naphthalene under no-NO_x conditions; markers are coloured according to reaction mixture (Nap+OH, Nap+OH+SO_2, Nap+OH+Bz, and Nap+OH+SO_2+Bz).

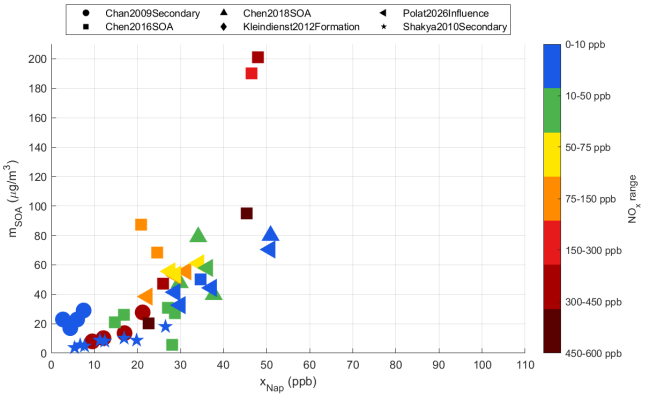


Figure S48. Comparison of this study with similar chamber studies investigating naphthalene oxidation with and without NO_x. SOA formation is shown as a function of the initial naphthalene concentration; the colour bar indicates the reported NO level.

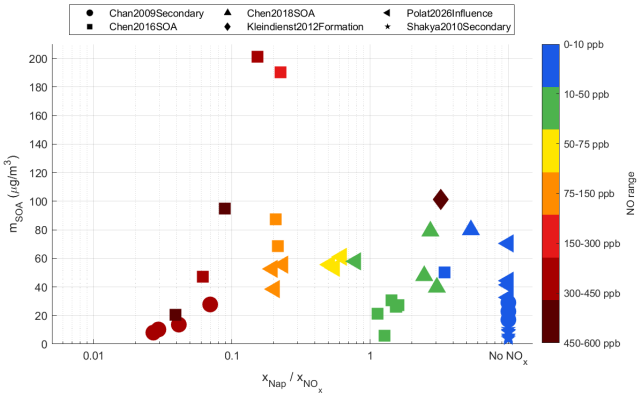


Figure S49. Comparison of this study with similar chamber studies investigating naphthalene oxidation. SOA formation is shown as a function of the initial naphthalene-to-NO ratio; the colour bar indicates the reported NO level.

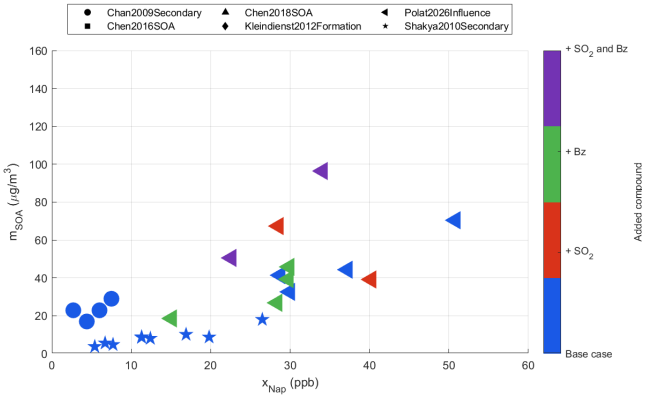


Figure S50. Comparison of this study with similar chamber studies investigating naphthalene oxidation under no-NO_x conditions. SOA formation is shown as a function of the initial naphthalene concentration; the colour bar indicates whether SO_2, benzene, or both were added.

References

Atkinson, R.: Kinetics and mechanisms of the gas-phase reactions of the hydroxyl radical with organic compounds under atmospheric conditions, Chemical Reviews, 86, 69–201, 1986.

Atkinson, R., Baulch, D., Cox, R., Hampson Jr, R., Kerr, J., Rossi, M., and Troe, J.: Evaluated kinetic and photochemical data for atmospheric chemistry: supplement VI. IUPAC subcommittee on gas kinetic data evaluation for atmospheric chemistry, Journal of Physical and Chemical Reference Data, 26, 1329–1499, https://doi.org/10.1063/1.556010, 1997.

Atkinson, R., Baulch, D. L., Cox, R. A., Crowley, J. N., Hampson, R. F., Hynes, R. G., Jenkin, M. E., Rossi, M. J., and Troe, J.: Evaluated kinetic and photochemical data for atmospheric chemistry: Volume I-gas phase reactions of O_x, HO_x, NO_x and SO_x species, Atmospheric chemistry and physics, 4, 1461–1738, 2004.

Baulch, D., Cobos, C., Cox, R., Esser, C., Frank, P., Just, T., Kerr, J., Pilling, M., Troe, J., Walker, R., et al.: Evaluated kinetic data for combustion modelling, Journal of Physical and Chemical Reference Data, https://doi.org/10.1063/1.555908, 1992.

Burkholder, J., Sander, S., Abbatt, J., Barker, J., Huie, R., Kolb, C., Kurylo, M., Orkin, V., Wilmouth, D., and Wine, P.: Chemical kinetics and photochemical data for use in atmospheric studies: evaluation number 18, Tech. rep., Pasadena, CA: Jet Propulsion Laboratory, National Aeronautics and Space . . . , 2015.

Chan, A. W. H., Kautzman, K. E., Chhabra, P. S., Surratt, J. D., Chan, M. N., Crounse, J. D., Kürten, A., Wennberg, P. O., Flagan, R. C., and Seinfeld, J. H.: Secondary organic aerosol formation from photooxidation of naphthalene and alkylnaphthalenes: implications for oxidation of intermediate volatility organic compounds (IVOCs), Atmospheric Chemistry and Physics, 9, 3049–3060, https://doi.org/10.5194/acp-9-3049-2009, 2009.

Chen, C.-L., Kacarab, M., Tang, P., and Cocker III, D. R.: SOA formation from naphthalene, 1-methylnaphthalene, and 2-methylnaphthalene photooxidation, Atmospheric Environment, 131, 424–433, 2016.

Chen, C.-L., Li, L., Tang, P., and Cocker III, D. R.: SOA formation from photooxidation of naphthalene and methylnaphthalenes with m-xylene and surrogate mixtures, Atmospheric Environment, 180, 256–264, 2018.

Goldstein, S., Aschengrau, D., Diamant, Y., and Rabani, J.: Photolysis of aqueous H_2O_2: quantum yield and applications for polychromatic UV actinometry in photoreactors, Environmental science & technology, 41, 7486–7490, https://doi.org/10.1021/es071379t, 2007.

Heard, D. E. and Pilling, M. J.: Measurement of OH and HO2 in the troposphere, Chemical reviews, 103, 5163–5198, 2003.

Keller-Rudek, H., Moortgat, G. K., Sander, R., and Sörensen, R.: The MPI-Mainz UV/VIS spectral atlas of gaseous molecules of atmospheric interest, Earth System Science Data, 5, 365–373, 2013.

Kleindienst, T. E., Jaoui, M., Lewandowski, M., Offenberg, J. H., and Docherty, K. S.: The formation of SOA and chemical tracer compounds from the photooxidation of naphthalene and its methyl analogs in the presence and absence of nitrogen oxides, Atmospheric Chemistry and Physics, 12, 8711–8726, 2012.

Seinfeld, J. H. and Pandis, S. N.: Atmospheric chemistry and physics: from air pollution to climate change, John Wiley & Sons, 2016.

Shakya, K. M. and Griffin, R. J.: Secondary organic aerosol from photooxidation of polycyclic aromatic hydrocarbons, Environmental science & technology, 44, 8134–8139, 2010.